TU Delft

Delft University of Technology

Document Version
Final published version

Licence
CC BY

Citation (APA)
Gámez Losada, F., Miller, O., Visser, P., & Heiligers, J. (2026). Characterization of multi-revolution circular-to-circular solar-sail transfers around planets. *Aerospace Science and Technology*, *178*, Article 113127. https://doi.org/10.1016/j.ast.2026.113127

Important note
To cite this publication, please use the final published version (if applicable).
Please check the document version above.

Copyright
In case the licence states “Dutch Copyright Act (Article 25fa)”, this publication was made available Green Open Access via the TU Delft Institutional Repository pursuant to Dutch Copyright Act (Article 25fa, the Taverne amendment). This provision does not affect copyright ownership.
Unless copyright is transferred by contract or statute, it remains with the copyright holder.

Sharing and reuse
Other than for strictly personal use, it is not permitted to download, forward or distribute the text or part of it, without the consent of the author(s) and/or copyright holder(s), unless the work is under an open content license such as Creative Commons.

Takedown policy
Please contact us and provide details if you believe this document breaches copyrights.
We will remove access to the work immediately and investigate your claim.

This work is downloaded from Delft University of Technology.

Aerospace Science and Technology 178 (2026) 113127

Contents lists available at ScienceDirect

Aerospace Science and Technology

journal homepage: www.elsevier.com/locate/aescte

Characterization of multi-revolution circular-to-circular solar-sail transfers around planets

Fernando Gámez Losada *, Oskar Miller, Pieter Visser, Jeannette Heiligers

Department of Astrodynanmics and Space Missions, Faculty of Aerospace Engineering, Delft University of Technology, Mekelweg 5, Delft, South Holland, 2628CD, The Netherlands

ARTICLE INFO

Communicated by Dr. Mehdi Ghoreyshi

Keywords:
Solar sailing
Planet-centered
Trajectory optimization
Circular-to-circular
Mission design

ABSTRACT

Significant research has addressed solar-sail transfers in heliocentric settings, whereas planet-centered transfers have received comparatively little attention. However, most solar-sail missions flown to date have operated in Earth-centered orbits and are likely to continue to do so, highlighting the importance of planet-centered sailing in the future of this new and promising technology. This work fully characterizes the co-planar multi-revolution circular-to-circular (MC2C) transfers, which enable motion between co-planar circular orbits and are therefore regarded as one of the "simplest" possible planet-centered solar-sail transfers. Using an indirect optimization approach, the performance of the MC2C transfers (i.e., achieved radius change in a fixed transfer time) is computed for various initial sun-orbit geometries. As a result, the best and worst transfer geometries (which depend on the illumination conditions of the orbital plane) are identified, enabling the construction of the performance envelopes that relate radius change to transfer time. These envelopes provide a simple graphical tool to obtain such metrics without having to optimize a single trajectory, greatly enhancing the workflow during early mission design. Through dimensional analysis, the envelopes are generalized to any sail design and any planet in the solar system, broadening their applicability. Finally, the explanation of the physical mechanisms behind the best and worst geometries is provided through new concepts that are unique to solar sailing, like the "growth vector". This explanation lies the foundation for the study of future, more complex planet-centered solar-sail transfers.

1. Introduction

While the majority of solar-sail transfer studies concentrate on heliocentric trajectories, nearly all flown solar-sail missions—IKAROS being the notable exception—have operated in Earth-centered orbits [1]. The recently launched ACS3 mission represents the latest example of this trend [2]. Nevertheless, our knowledge of planetocentric sailing remains limited: even the most basic circular-to-circular transfers are not yet fully understood.

Planet-centered solar-sail trajectories can be broadly divided into two categories: *open-ended* trajectories, which do not terminate in a prescribed bound orbit (e.g., escape trajectories [3–5], orbit raising [6,7], and inclination change maneuvers [8]); and *orbit-to-orbit* transfers, in which the sailcraft starts and ends in well-defined bound orbits around the planet [e.g., transfers from geosynchronous transfer orbit (GTO) to geosynchronous equatorial orbit (GEO) [9], transfers from GEO to a graveyard orbit [10], and transfers in low Earth orbit (LEO) [11]]. Open-ended trajectories have been studied extensively [3–8]; orbit raising and inclination change maneuvers are well understood. Differently, many of the studies concerning orbit-to-orbit transfers often consider specific examples or do not provide a clear explanation of the physical mechanisms behind the optimized trajectories [9–13]. It is common to see plots of the evolution of optimal control laws in these works, but often, little insight into mission design can be derived from them. Our aim with our current line of research is to enlarge the pool of knowledge concerning orbit-to-orbit transfers by fully characterizing one of the simplest transfers: the co-planar circular-to-circular transfer. Such a transfer was the object of study of the first astrodynamicists, resulting in the well-known Hohmann transfer. We want to follow the same steps and fully understand the intricacies of the circular-to-circular transfer when flown with solar-sail propulsion to enable mission designers to make informed decisions during early mission design. As with Hohmann transfers, we believe that solar-sail circular-to-circular transfers will become a staple maneuver for any planet-bound solar-sail mission.

In this paper we use indirect optimization to fully characterize the co-planar MC2C solar-sail transfers, which, in theory, enable motion

* Corresponding author.
E-mail addresses: F.GamezLosada@tudelft.nl (F. Gámez Losada), Oskar.Miller2001@gmail.com (O. Miller), P.N.A.M.Visser@tudelft.nl (P. Visser), M.J.Heiligers@tudelft.nl (J. Heiligers).

https://doi.org/10.1016/j.ast.2026.113127
Received 8 April 2026; Received in revised form 23 June 2026; Accepted 2 July 2026
Available online 4 July 2026
1270-9638/© 2026 The Author(s). Published by Elsevier Masson SAS. This is an open access article under the CC BY license (http://creativecommons.org/licenses/by/4.0/).

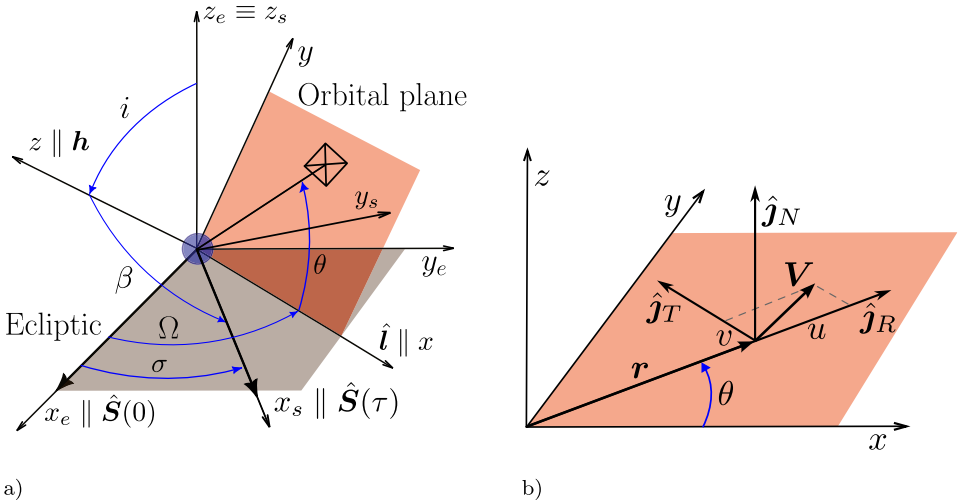


Fig. 1. Schematics of: a) the ecliptic frame $\mathcal{E}(x_e, y_e, z_e)$, the orbital frame $\mathcal{I}(x, y, z)$, and the sunlight frame $\mathcal{S}(x_s, y_s, z_s)$; and b) the local frame $\mathcal{L}(\hat{\boldsymbol{\jmath}}_R, \hat{\boldsymbol{\jmath}}_T, \hat{\boldsymbol{\jmath}}_N)$, and the polar coordinates used in the EOMs.

between any two co-planar circular orbits. The optimization of planet-centered solar-sail transfers is not a trivial task. First, the trajectories are lengthy and multi-revolution due to the low control authority of the sail; the small thrust levels imply that long time-spans are needed to achieve meaningful orbital changes. This leads to complex, high-dimensional trajectory optimization problems. Secondly, the solar-sail thrust is inherently more difficult to handle than the ion-drive thrust [14]; the thrust magnitude in the former is coupled with the attitude of the sail, whereas in the latter, it can be varied at will by throttling the engine. Furthermore, the solar-sail thrust is asymmetric in nature (i.e., no thrust can be generated towards the sun), while an ion drive can virtually be pointed anywhere in three-dimensional space. Lastly, planetocentric solar-sail transfers depend on two different time-scales (i.e., the orbital period and the yearly motion of the sun around the planet) due to the dependency of the solar-sail thrust on the direction of sunlight, which renders the problem non-autonomous [9,13].

To overcome the challenges of planetocentric sailing, we turned our attention to indirect methods, which leverage the calculus of variations and Pontryagin's maximum principle to reduce the optimal control problem into a finite-dimensional two-point boundary value problem (TPBVP) [12,15,16]. The size of this TPBVP is fixed (six in this study) and independent of the length of the transfer: a very attractive quality for many-revolution transfers. Historically, indirect methods have proven to be highly sensitive to the initial guess of the co-states, which limited practical application [17]. However, in [18], Miller demonstrates that indirect optimization is capable of handling solar-sail planet-centered transfers with thousands of revolutions, all starting from a trivial initial guess. Please refer to [18] for a detailed analysis of the convergence properties of the indirect software. To produce the results presented in this work, hundreds of very different MC2C transfers were successfully optimized following the indirect approach, which inclines us to think that indirect methods (or hybrids) might be the future of optimal planet-centered sailing.

The remainder of the paper is organized as follows. Section 2 describes the reference frames and equations of motion used in the study. Section 3 formulates the indirect optimization problem behind the MC2C transfers. Section 4 poses the problem in dimensionless units to find equivalences between the planets in the solar system. Section 5 finds the conditions for the best and worst transfer geometries. Section 6 presents the performance envelopes for an ACS3-like sail in the GEO region. Section 7 explains the extrapolation method that is used to generalize the aforementioned performance envelopes to any sail design and orbital region. Section 8 discuss the limitations of this work. Finally, Section 9 gathers the conclusions drawn throughout this article.

2. Dynamics

2.1. Reference frames

To describe the transfers analyzed in this study, we make use of four different reference frames: the ecliptic frame $\mathcal{E}(x_e, y_e, z_e)$, the orbital frame $\mathcal{I}(x, y, z)$, the sunlight frame $\mathcal{S}(x_s, y_s, z_s)$, and the local frame $\mathcal{L}(\hat{\boldsymbol{\jmath}}_R, \hat{\boldsymbol{\jmath}}_T, \hat{\boldsymbol{\jmath}}_N)$. Fig. 1 gathers two schematics depicting all frames and their relations relative to one another: Fig. 1a shows frames $\mathcal{E}$, $\mathcal{I}$ and $\mathcal{S}$, together with the ecliptic and orbital planes; Fig. 1b shows frames $\mathcal{I}$ and $\mathcal{L}$, together with the definition of various variables and angles required to formulate the EOMs. The following list presents the detailed definition of each reference frame:

1) The ecliptic reference frame $\mathcal{E}(x_e, y_e, z_e)$ is centered at the planet, with the x_e-axis aligned with the direction of sunlight $\hat{\boldsymbol{S}}$ at the initial epoch (i.e., autumn equinox), the z_e-axis pointing towards the ecliptic north pole, and the y_e-axis completing the right-handed triad [i.e., the (x_e, y_e)-plane is co-planar with the ecliptic plane]. Frame $\mathcal{E}$ is an inertial frame used to define the geometry of the orbital plane via the ecliptic right ascension of the ascending node (RAAN) Ω and the inclination with respect to the ecliptic i.

2) The orbital reference frame $\mathcal{I}(x, y, z)$ is also centered at the planet (see Fig. 1a), with the x-axis aligned with the line of nodes of the orbit $\hat{\boldsymbol{\imath}}$, the z-axis parallel to the orbit's angular momentum vector $\boldsymbol{h}$, and the y-axis completing the right-handed triad. The orbital frame is used to formulate the EOMs and characterize the transfers from the perspective of the orbital plane. Because no perturbations are considered in this study, the orbital plane is fixed in inertial space. In other words, the orbital frame is inertial.

3) The sunlight reference frame $\mathcal{S}(x_s, y_s, z_s)$ is centered at the sailcraft (in Fig. 1a it is centered at the planet to better show angular relations, while in Fig. 2a it is shown centered at the sailcraft). The x_s-axis is aligned with the sun-planet line $\hat{\boldsymbol{S}}$, the z_s-axis points towards the ecliptic north pole (i.e., z_e and z_s are parallel), and the y_s-axis completes the right-handed triad. The sunlight frame rotates counterclockwise with respect to the ecliptic frame (around the z_e-axis), completing one full rotation every year. Note that the motion of the sun around the planet is characterized by the angle σ, which is the angle between the x_e-axis and the $\hat{\boldsymbol{S}}$ vector. In this study, we use the word "year" to refer to one full orbital revolution of the planet about the sun; the orbital period of the planet is denoted as P. In addition, we assume that the sun is infinitely far from the planet, rendering all sun-rays parallel; the field of light around the sailcraft is therefore fully characterized by the sun-planet line $\hat{\boldsymbol{S}}$. The sunlight frame is used to formulate the solar-sail accelera-

tion $\boldsymbol{a_s}$ in terms of the classical control variables: the cone angle α, and the clock angle δ (see Fig. 2a). The cone angle is the angle between the x_s-axis and the unit vector normal to the surface of the sail $\hat{\boldsymbol{n}}$. The clock angle is the angle between the projection of $\hat{\boldsymbol{n}}$ onto the (y_s, z_s)-plane and the z_s-axis.

4) The local reference frame $\mathcal{L}(\hat{\jmath}_R, \hat{\jmath}_T, \hat{\jmath}_N)$ is centered at the sailcraft: the radial unit vector $\hat{\jmath}_R$ is aligned with the radius vector $\boldsymbol{r}$, the out-of-plane unit vector $\hat{\jmath}_N$ is aligned with the angular momentum vector of the orbit $\boldsymbol{h}$, and the transversal unit vector $\hat{\jmath}_T$ completes the right-handed triad. The local frame is used to express the components of the velocity vector and the components of the solar-sail acceleration in polar coordinates.

To end with, let us introduce the aspect angle β, which is defined as the angle between the sun-planet direction $\hat{\boldsymbol{S}}$ and the angular momentum vector $\boldsymbol{h}$ (see Fig. 1a). The aspect angle is of paramount importance to planetocentric solar-sail transfers, as it determines the illumination conditions of the orbital plane: for $\beta = 0$ deg and $\beta = 90$ deg, the orbit is perpendicular and parallel to the incoming sunlight, respectively. If we consider the analogy with a sailboat, the aspect angle would determine the wind direction in the orbital plane. Note that, for an inertially fixed orbit, the aspect angle changes periodically due to the yearly motion of $\hat{\boldsymbol{S}}$ [19].

2.2. Equations of motion

We use polar coordinates to describe the two-dimensional motion of the sailcraft in the orbital plane. Using the coordinates depicted in Fig. 1b, the state vector expands as $\boldsymbol{x} = [r, \theta, u, v]^\top \in \mathbb{R}^4$, where r is the radial distance, θ is the argument of latitude, and u and v are the radial and tangential components of the velocity vector in the local frame, respectively. The time derivative of the state vector is $\dot{\boldsymbol{x}} = \boldsymbol{f}(\boldsymbol{x}, \boldsymbol{y}, t)$, where the dynamics function $\boldsymbol{f}(\cdot) : \mathbb{R}^4 \times \mathcal{Y} \times \mathbb{R} \to \mathbb{R}^4$ explicitly depends on the vector of control variables $\boldsymbol{y} = [\alpha, \delta]^\top \in \mathcal{Y}$ and the independent variable time t. The domain of $\boldsymbol{y}$, denoted by $\mathcal{Y}$, is expressed as $\mathcal{Y} = \{[\alpha, \delta]^\top \mid 0 \leq \alpha \leq \pi/2, -\pi \leq \delta \leq \pi\}$. To enhance numerical stability and convergence of the indirect optimization, we perform a Sundman transformation where the independent variable t is replaced by the argument of latitude θ. The state vector and dynamics function are re-defined as $\boldsymbol{x} = [r, t, u, v]^\top$ and $\overset{\circ}{\boldsymbol{x}} = \boldsymbol{f}(\boldsymbol{x}, \boldsymbol{y}, \theta)$, where $\overset{\circ}{\square}$ indicates derivative with respect to θ.

In this study, we consider the simplest possible dynamical model for the motion of the solar sail around a planet. Only two accelerations are taken into account: point-mass gravity, and the solar-sail acceleration. Although more complex models exist (e.g., including third-body perturbations, Earth's oblateness), the aim of this work is to unveil the main characteristics of the MC2C transfers, not to obtain high fidelity results. Under these assumptions, the dynamics function reads as:

$$\boldsymbol{f} = \frac{r}{v}\left[u,\ 1,\ \frac{v^2}{r} - \frac{\mu}{r^2} + a_{s_R},\ -\frac{uv}{r} + a_{s_T}\right]^\top \tag{1}$$

where r/v is the Sundman transformation factor, μ is the planet's gravitational constant, and a_{s_R} and a_{s_T} are the radial and traversal components of the solar-sail acceleration in the local frame, respectively. As we shall see in the following paragraphs, the dependencies with respect to the control variables and the independent variable θ are introduced via the explicit formulation of a_{s_R} and a_{s_T}.

The solar-sail acceleration $\boldsymbol{a_s}$ is modeled using the ideal sail model. This model assumes the sail's film to be a perfectly reflective flat mirror. Under these assumptions, $\boldsymbol{a_s} = a_0(\hat{\boldsymbol{S}} \cdot \hat{\boldsymbol{n}})^2\, \hat{\boldsymbol{n}}$, where a_0 is the sail's characteristic acceleration, which is the maximum acceleration generated by the sail when the sail is placed perpendicular to the incoming sunlight. The characteristic acceleration can be computed as $a_0 = 2p\, A/m$, where p is the solar radiation pressure at the sailcraft position, and A/m is the area to mass ratio of the sailcraft. The solar radiation pressure depends on the sun-sail distance. However, in this study we assume that it is constant and equal to the solar radiation pressure at the average heliocentric distance of the planet under consideration (e.g., $p = .0045598$ $\mathrm{kg\,s^{-2}\,km^{-1}}$ for the Earth at one astronomical unit [14]). Most of the example trajectories discussed in this paper are computed around Earth for an ACS3-like solar sail with $A/m = 5.5$ $\mathrm{m^2/kg}$ and $a_0 = 0.05$ $\mathrm{mm/s^2}$ [2]. These values represent the current state of the art of solar-sail technology, see values for A/m and a_0 of previous missions in [1].

The components of the solar-sail acceleration in the sunlight frame $\mathcal{S}$ can be expressed as a function of the cone α and clock δ angles as follows:

$$[\boldsymbol{a_s}]_{\mathcal{S}} = a_0 \cos^2\alpha \left[\cos\alpha,\ \sin\alpha\sin\delta,\ \sin\alpha\cos\delta\right]^\top \tag{2}$$

where $[\square]_{\mathcal{S}}$ is used to indicate that the components of the vector are expressed in frame $\mathcal{S}$. However, for substitution into Eq. (1), we need the components of the solar-sail acceleration in the local frame $[\boldsymbol{a_s}]_{\mathcal{L}} = [a_{s_R}, a_{s_T}, a_{s_N}]^\top$, which introduces the following rotation:

$$[\boldsymbol{a_s}]_{\mathcal{L}} = \mathrm{Q}_{\mathcal{L}\mathcal{S}}[\boldsymbol{a_s}]_{\mathcal{S}} \tag{3}$$

where $\mathrm{Q}_{\mathcal{L}\mathcal{S}}$ is the rotation matrix from frame $\mathcal{S}$ to frame $\mathcal{L}$. The rotation matrix is obtained as a sequence of single-axis rotations, see Fig. 1a:

$$\mathrm{Q}_{\mathcal{L}\mathcal{S}} = \mathrm{R}_3(\theta)\,\mathrm{R}_1(i)\,\mathrm{R}_3(\Omega - \sigma) \tag{4}$$

where $\mathrm{R}(\cdot)_{\square}$ denotes the rotation matrix of a reference frame by the angle specified in the argument about the axis specified in the subscript [e.g., $\mathrm{R}_3(\theta)$ represents a rotation about the instantaneous third axis (here, the z-axis of frame $\mathcal{I}$) over an angle θ]. Note that the EOMs are rendered non-autonomous because of the angle σ in the first rotation in the sequence. Recall that σ is the angular location of the sun-planet direction $\hat{\boldsymbol{S}}$ (see Fig. 1a), which depends on time as $\sigma = (2\pi/P)\,t$. Although we use θ as the independent variable, time can be retrieved from the second component of the re-defined state vector and used to compute the current value for σ. In this work, we always consider the initial time to be the autumn equinox, so that at the initial time, $\sigma = 0$ [i.e., $\hat{\boldsymbol{S}}(0)$ is always parallel to x_e, see Fig. 1a].

Now, given a control input $\boldsymbol{y}(\theta) = [\alpha(\theta), \delta(\theta)]^\top$ defined in the argument of latitude interval $[\theta_0, \theta_f]$, a set of initial conditions $\boldsymbol{x}(\theta_0) = [r(\theta_0), 0, u(\theta_0), v(\theta_0)]^\top$, a planet with gravitational constant μ and orbital period P, a sail with characteristic acceleration a_0, and an orbit with Ω and i, Eqs. (1)–(4) can be numerically integrated in argument of latitude from θ_0 to θ_f to yield the sailcraft trajectory in frame $\mathcal{I}$. Therefore Eqs. (1)–(4) constitute the EOMs of the sailcraft.

3. Indirect optimization

The MC2C transfers are computed by optimizing the radius change $\Delta r = r_f - r_0$ over a given transfer duration while enforcing zero eccentricity at the final state. The obtained radius change after convergence is used as the performance metric to compare MC2C transfers. Mathematically, the MC2C transfers arise as the solution of the following optimization problem:

$$r_f^* = \min_{\boldsymbol{y}\in\mathcal{Y}} -\mathtt{sign}(\Delta r)\, r_f \tag{5a}$$

subject to:

$$\overset{\circ}{\boldsymbol{x}} = \boldsymbol{f}(\boldsymbol{x}, \boldsymbol{y}, \theta) \tag{5b}$$

$$\boldsymbol{x_0} = \left[r_0, 0, 0, \sqrt{\frac{\mu}{r_0}}\right]^\top \qquad \boldsymbol{\psi} = \left[u_f,\ v_f - \sqrt{\frac{\mu}{r_f}}\right]^\top = \boldsymbol{0} \tag{5c}$$

where $\mathtt{sign}(\cdot)$ is the sign function, $\boldsymbol{\psi}(\boldsymbol{x}_f) : \mathbb{R}^4 \to \mathbb{R}^2$ is the terminal dynamics constraint function that enforces the final boundary conditions, and the subscripts $\square_0$ and $\square_f$ refer to quantities at the initial and final arguments of latitude θ_0 and θ_f, respectively. The initial conditions in Eq. (5c)-left ensure that the initial orbit is circular, whereas the constraint function in Eq. (5c)-right enforces the zero-eccentricity boundary condition at the final state. The sign function returns positive when optimizing an ascent transfer ($\Delta r > 0$), and negative when optimizing a descent transfer ($\Delta r < 0$).

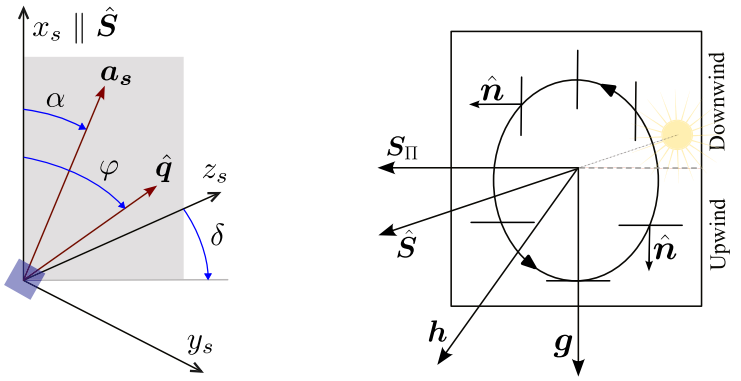


Fig. 2. Schematics of: a) the solar-sail acceleration $\boldsymbol{a}_s$ and the primer vector $\hat{\boldsymbol{q}}$ in frame $\mathcal{S}$; and b) the "downwind" and "upwind" regions in the orbital plane and the vectors involved in the definition of the growth vector $\boldsymbol{g}$.

Typically, in transfer problems, the target orbit is used as a terminal constraint [9]. In this work, we use the final radius as the objective function (see Eq. (5a)) rather than a terminal constraint, and optimize the final radius in a fixed transfer duration. This simplifies the problem to a finite horizon optimal control problem [20]. In our experience, multi-revolution transfer problems are better formulated as finite-horizon optimal control problems. Leaving the final epoch as a free variable to be optimized remains a challenging topic that needs further research.

We follow an indirect approach to solve the optimization problem in Eq. (5). To simplify the notation, we are going to formulate the problem for ascent transfers only. The extension to descent transfers is trivial and is left for the reader. For ascent transfers, the objective function to be minimized is $J = -r_f$. In a similar fashion to the Lagrange optimization method, the dynamics (Eq. (5b)) and terminal (Eq. (5c)-right) constraints are adjoined to the cost function using auxiliary variables called multipliers, yielding the augmented cost function [15]:

$$\tilde{J} = -r_f + \boldsymbol{\gamma} \cdot \boldsymbol{\psi}(\boldsymbol{x}_f) + \int_{\theta_0}^{\theta_f} \boldsymbol{\lambda} \cdot (\boldsymbol{f}(\boldsymbol{x}, \boldsymbol{y}, \theta) - \mathring{\boldsymbol{x}})\, \mathrm{d}\theta \tag{6}$$

where $\boldsymbol{\gamma} = [\gamma_1, \gamma_2]^\top \in \mathbb{R}^2$ is a vector of constant Lagrange multipliers, and $\boldsymbol{\lambda} = [\lambda_r, \lambda_t, \lambda_u, \lambda_v]^\top \in \mathbb{R}^4$ is the costate vector, whose components are the costates associated with each one of the states in $\boldsymbol{x}$. According to the calculus of variations, the optimal solution to the (ascent) problem in Eq. (5) is a stationary point of $\tilde{J}$. For a trajectory to be a stationary point of $\tilde{J}$, it must satisfy several mathematical conditions, referred to as necessary conditions for optimality [15]: 1) the dynamics of the state and costate must follow from the Euler-Lagrange equations, 2) the optimal control input must satisfy Pontryagin's maximum principle, and 3) the costate final boundary conditions must arise from the transversality conditions. Once applied, these conditions transform the optimization problem in Eq. (5) into a TPBVP, whose solution is an optimal solution to Eq. (5). The following subsections elaborate on the application of each condition to our problem and the resulting TPBVP.

3.1. Euler-lagrange equations

The auxiliary Hamiltonian function $H(\boldsymbol{x}, \boldsymbol{\lambda}, \boldsymbol{y}, \theta) = \boldsymbol{\lambda} \cdot \boldsymbol{f}(\boldsymbol{x}, \boldsymbol{y}, \theta) : \mathbb{R}^4 \times \mathbb{R}^4 \times \mathcal{Y} \times \mathbb{R} \to \mathbb{R}$ is used to write the Euler-Lagrange equations [15]:

$$\mathring{\boldsymbol{x}} = \frac{\partial H}{\partial \boldsymbol{\lambda}} \qquad \mathring{\boldsymbol{\lambda}} = -\frac{\partial H}{\partial \boldsymbol{x}} \tag{7}$$

where Eq. (7)-left is equivalent to Eqs. (5b) and (7)-right dictates the costate dynamics. Note that, given initial state and costate vectors (i.e., $\boldsymbol{x_0}$ and $\boldsymbol{\lambda_0} = [\lambda_{r_0}, \lambda_{t_0}, \lambda_{u_0}, \lambda_{v_0}]^\top$), and a control law $\boldsymbol{y}(\theta)$, Eq. (7) can be integrated in true anomaly to give the trajectory and costates of the sailcraft. Now, to obtain the optimal control input $\boldsymbol{y}^*$ that renders $\tilde{J}$ stationary and produces and optimal trajectory, we need to apply Pontryagin's maximum principle.

3.2. Pontryagin's maximum principle

Pontryagin's maximum principle states that the optimal control input $\boldsymbol{y}^*$ must minimize the Hamiltonian at each point along the trajectory [15]:

$$\boldsymbol{y}^* = \arg\min_{\boldsymbol{y} \in \mathcal{Y}} H(\boldsymbol{x}, \boldsymbol{\lambda}, \boldsymbol{y}, \theta) \tag{8}$$

where $\mathcal{Y}$ is the domain of feasible control variables. To solve the optimization problem in Eq. (8), we isolate the part of the Hamiltonian that depends on the control variables, yielding:

$$\boldsymbol{y}^* = \arg\max_{\boldsymbol{y} \in \mathcal{Y}} [\hat{\boldsymbol{q}}]_{\mathcal{L}}^\top [\boldsymbol{a}_s(\boldsymbol{y})]_{\mathcal{L}} = \arg\max_{\boldsymbol{y} \in \mathcal{Y}} \hat{\boldsymbol{q}} \cdot \boldsymbol{a}_s(\boldsymbol{y}) \tag{9}$$

where $[\hat{\boldsymbol{q}}]_{\mathcal{L}} = [-\lambda_u, -\lambda_v, 0]^\top / \sqrt{\lambda_u^2 + \lambda_v^2}$ is a unit vector expressed in frame $\mathcal{L}$; vector $\hat{\boldsymbol{q}}$ is often referred to in the literature as the primer vector direction [16,21]. Eq. (9) imposes that in an optimal trajectory, the projection of the solar-sail acceleration along the primer vector direction must be maximized at all times.

In [14], McInnes presents the required formulae that compute the optimal cone and clock angles, α^* and δ^*, to maximize the projection of the solar-sail acceleration along a given unit vector direction, exactly what is needed to solve Eq. (9) and applied below. Fig. 2a shows a schematic of the vectors and angles involved in the solution of Eq. (9) in frame $\mathcal{S}$. To ensure optimality, the vectors $\hat{\boldsymbol{S}}$, $\hat{\boldsymbol{q}}$, and $\boldsymbol{a}_s$ need to be co-planar (the grey plane in Fig. 2a) [21], which forces the optimal clock angle δ^* to be equal to the clock angle of the primer vector:

$$\delta^* = \mathtt{arctan2}\left(q_{y_s}, q_{z_s}\right) \tag{10}$$

where $\mathtt{arctan2}(\square, \square)$ represents the four-quadrant inverse tangent and q_{y_s} and q_{z_s} are the second and third components of $[\hat{\boldsymbol{q}}]_{\mathcal{S}}$, which is obtained from $[\hat{\boldsymbol{q}}]_{\mathcal{L}}$ as:

$$[\hat{\boldsymbol{q}}]_{\mathcal{S}} = \mathrm{Q}_{\mathcal{SL}} [\hat{\boldsymbol{q}}]_{\mathcal{L}} \tag{11}$$

where $\mathrm{Q}_{\mathcal{SL}} = \mathrm{Q}_{\mathcal{LS}}^\top$ is the rotation matrix from frame $\mathcal{L}$ to frame $\mathcal{S}$ (see Eq. (4)). To compute the optimal cone angle α^*, first we need to compute the cone angle of the primer vector φ as:

$$\varphi = 2\,\mathtt{arctan2}\left(\|\hat{\boldsymbol{q}} - \hat{\boldsymbol{S}}\|, \|\hat{\boldsymbol{q}} + \hat{\boldsymbol{S}}\|\right) \tag{12}$$

where $\|\square\|$ represents the Euclidean norm of a vector. Eq. (12) offers more numerical stability for small angles than the inverse cosine function. Then, the optimal cone angle is obtained from φ as:

$$\alpha^* = \frac{1}{2}\left[\varphi - \arcsin\left(\frac{\sin\varphi}{3}\right)\right] \tag{13}$$

Eqs. (10)–(13) solve the optimization problem in Eq. (9), thus satisfying Pontryagin's maximum principle. In practice, Eqs. (10)–(13) allow to express the optimal control input $\boldsymbol{y}^*$ as a function of the costates (i.e., $\boldsymbol{y}^*(\boldsymbol{\lambda})$), removing the explicit dependency of $\boldsymbol{y}^*$ from the state and costate dynamics.

3.3. Transversality conditions

Eq. (5c)-right imposes the final boundary conditions of the state. Similarly, the transversality conditions enforce the final boundary conditions of the costate. Following the methodology in [15], we define the auxiliary terminal function $\Phi(\boldsymbol{x}_f, \boldsymbol{\gamma}) = -r_f + \boldsymbol{\gamma} \cdot \boldsymbol{\psi}$. The final boundary conditions of the costate are derived from the terminal function via partial differentiation as $\boldsymbol{\chi} = \boldsymbol{\lambda}_f - \partial\Phi/\partial\boldsymbol{x} = \boldsymbol{0}$, where $\boldsymbol{\chi}(\boldsymbol{x}_f, \boldsymbol{\lambda}_f, \boldsymbol{\gamma}) : \mathbb{R}^4 \times \mathbb{R}^4 \times \mathbb{R}^2 \to \mathbb{R}^4$ is the terminal costate constraint function. Taking the partial derivatives yields:

$$\boldsymbol{\chi} = \left[\lambda_{r_f} - \left(-1 + \frac{1}{2}\gamma_2\sqrt{\frac{\mu}{r_f^3}}\right), \quad \lambda_{t_f}, \quad \lambda_{u_f} - \gamma_1, \quad \lambda_{v_f} - \gamma_2\right]^\top = \boldsymbol{0} \tag{14}$$

We can see from the last two entries of the vector in Eq. (14) that the multipliers γ_1 and γ_2 actually represent the final values for the velocity costates. Eq. (14) is the explicit application of the transversality conditions for our problem and completes the mathematical definition of the TPBVP.

3.4. Solution method

The TPBVP is solved using a single shooting method. For a given guess of the four initial costates $\boldsymbol{\lambda}_0$ and the two terminal multipliers $\boldsymbol{\gamma}$, the state–costate dynamics (Eqs. (5b) and (7)-right) are integrated from θ_0 to θ_f. At the final state, the two terminal dynamics constraints (Eq. (5c)-right) and the four terminal costate constraints (Eq. (14)) are assembled into a six-component residual. The root of this residual, which is found by informed iterative updates of the initial guess, yields the optimal solution $\boldsymbol{\lambda}_0^*$ and $\boldsymbol{\gamma}^*$.

To formalize the TPBVP, the unknowns are collected into a single solution vector $\boldsymbol{\Lambda} = [\boldsymbol{\lambda}_0^\top, \boldsymbol{\gamma}^\top]^\top \in \mathbb{R}^6$. Then, the residual function can be written as $\boldsymbol{F}(\boldsymbol{\Lambda}) = [\boldsymbol{\psi}^\top, \boldsymbol{\chi}^\top]^\top \in \mathbb{R}^6$. The solution $\boldsymbol{\Lambda}^*$ to the non-linear root finding problem $\boldsymbol{F}(\boldsymbol{\Lambda}) = \boldsymbol{0}$ is a solution to the original optimization problem in Eq. (5). More precisely, the optimal trajectory is obtained by propagating $\boldsymbol{x}_0$ and $\boldsymbol{\lambda}_0^*$ from θ_0 to θ_f. The optimal control $\boldsymbol{y}^*$ is retrieved from the optimal evolution of the velocity costates (i.e., from the optimal evolution of the primer vector).

The described single shooting method is implemented in Python: Diffrax is used for numerical integration [22], JAX is used for automatic differentiation [23], and the SciPy function `fsolve` is used for solving the root finding problem [24]. The state-costate dynamics are integrated with an explicit variable step-size eighth-order Runge–Kutta method (`Dopri8` with `PIDController` in Diffrax), where the relative and absolute integration tolerances are set to 10^{-12}. Automatic differentiation with JAX is used to compute the costate dynamics from the Hamiltonian (Eq. (7)-right). Lastly, the root-finding tolerance of `fsolve` is set to 10^{-10}. The code is available in [25] and was validated against solutions computed with a direct solver [18].

4. Equivalence between planets

The optimization problem in Section 3 depends on the planet (μ and P), the initial orbit (r_0, i, and Ω), and the sail design (a_0). When written as a function of these physical parameters, the optimization problem is specific to each planet. To generalize the problem to any planet orbiting a star, this section reformulates the optimization problem in dimensionless units, resulting in a new set of dimensionless parameters.

First, the EOMs and the optimization problem are presented in dimensionless units and the conditions for equivalence between planets are analyzed. Then, the so-called "control footprint" is introduced, which is a key concept to ensure equivalent trajectories. To end with, an example of two equivalent transfers around Earth and Mars is discussed and the table gathering the equivalence ratios for all planets in the solar system is presented.

4.1. Dimensionless equations of motion

For the subsequent analysis, it is convenient to formulate the EOMs in terms of the position vector $\boldsymbol{r}$ and the velocity vector $\boldsymbol{V}$ (see Fig. 1b). With these variables, the acceleration of the sailcraft reads as:

$$\frac{\mathrm{d}\boldsymbol{V}}{\mathrm{d}t} = -\frac{\mu}{r^3}\boldsymbol{r} + a_0\left(\hat{\boldsymbol{S}} \cdot \hat{\boldsymbol{n}}\right)^2\hat{\boldsymbol{n}} \tag{15}$$

where the first and second terms on the right-hand side are the point mass and solar-sail accelerations, respectively. To make Eq. (15) dimensionless, the position and velocity vectors are scaled with the initial position r_0 and initial circular velocity $v_0 = \sqrt{\mu/r_0}$ as $\boldsymbol{\rho} = \boldsymbol{r}/r_0$ and $\boldsymbol{\xi} = \boldsymbol{V}/v_0$, respectively. In addition, time is substituted by time in years $\tau = t/P$ (i.e., $\tau \in [0, 1]$ during one year). With these changes, the scaled acceleration becomes:

$$\frac{\mathrm{d}\boldsymbol{\xi}}{\mathrm{d}\tau} = \Sigma_0\left(-\frac{\boldsymbol{\rho}}{\rho^3} + \Psi_0\,\boldsymbol{u}\right) \tag{16}$$

where $\Sigma_0 = Pv_0/r_0$, $\Psi_0 = a_0/g_0$ with $g_0 = \mu/r_0^2$, and $\boldsymbol{u} = (\hat{\boldsymbol{S}} \cdot \hat{\boldsymbol{n}})^2\hat{\boldsymbol{n}}$. Let us discuss these three parameters one by one:

1) Σ_0 can be re-written as $\Sigma_0 = 2\pi P/T_0$, where $T_0 = 2\pi\sqrt{r_0^3/\mu}$ is the initial orbital period. In this form, Σ_0 represents the number of revolutions in radians that the sailcraft would complete in one year if left unperturbed in the initial orbit. Hence, Σ_0 increases as the orbital radius decreases. The larger Σ_0, the more impact the control has over the trajectory: for two trajectories with the same $\Delta\tau$, the trajectory with the largest Σ_0 completes more orbital revolutions, providing the control with more trajectory arc length to exert its influence.

2) Ψ_0 was first introduced in [26] as the scaled characteristic acceleration. It represents the "strength" of the sail relative to the gravitational acceleration of the planet at the initial orbit g_0. Large values of Ψ_0 indicate that the sail has significant control authority and hence a large influence on the trajectory. Conversely, when Ψ_0 is small, the trajectory appears as a slowly evolving Keplerian osculating orbit.

3) $\boldsymbol{u}$ is the control vector, which represents the solar-sail acceleration scaled with the magnitude of the maximum achievable solar-sail acceleration (i.e., a_0 in the ideal case). Hence, the magnitude of $\boldsymbol{u}$ is bounded to $[0, 1]$. The domain of feasible control vectors is denoted by $\mathcal{U}$. Section 4.3 elaborates on the characteristics of $\mathcal{U}$.

4.2. Dimensionless optimization problem

The (ascent) optimization problem in Eq. (5) can be written in scaled units in compact form as:

$$\rho_f^* = \max_{\boldsymbol{u}\in\mathcal{U}}\left[\rho_f\right] \text{ s.t. EOMs } \&\ e_f = 0, \tag{17}$$

where e represents the osculating eccentricity and "s.t." stands for "subject to". Two optimization problems are equivalent in scaled units [i.e., yield the same $\Delta\rho = \rho_f - \rho_0$ using the same control $\boldsymbol{u}(\tau)$] only if they: 1) have the same scaled EOMs with the same scaled initial conditions, 2) have the same transfer time $\Delta\tau = \tau_f - \tau_0$, and 3) have the same set of feasible controls $\mathcal{U}$.

To have the exact same scaled EOMs, the dimensionless parameters Σ_0 and Ψ_0 must be the same; these parameters depend on the planet (μ, P), the performance of the solar sail a_0, and the initial radius r_0. To have the same scaled initial conditions, the only requirement is to have the same initial argument of latitude θ_0, inasmuch as $\boldsymbol{\rho}$ and $\boldsymbol{\xi}$ are always $[\boldsymbol{\rho}]_{\mathcal{L}} = [1, 0, 0]^\top$ and $[\boldsymbol{\xi}]_{\mathcal{L}} = [0, 1, 0]^\top$. To have the same transfer time, τ_f and τ_0 must be the same; in other words, the sun-planet line must start and end at the same angular locations σ_0 and σ_f relative to the ecliptic frame $\mathcal{E}$ (see Fig. 1a). Finally, to have the same set of feasible

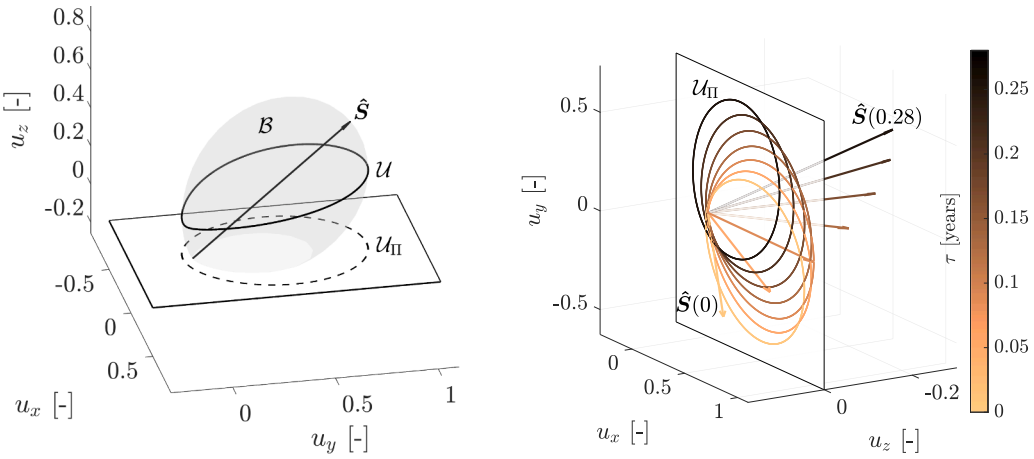


Fig. 3. Sail "bubble" examples in frame $\mathcal{I}$: a) snapshot of the bubble $\mathcal{B}$ and set of feasible controls $\mathcal{U}$ for $\tau = 0$, $\Omega = 90$ deg, and $i = 140$ deg; and b) evolution of $\mathcal{U}_\Pi$ (i.e., control footprint) for a transfer with $\Delta\tau = 0.28$ years, $\Omega = 30$ deg, and $i = 60$ deg.

controls, the orbital geometry defined by Ω and i must be the same; the next subsection explains this condition in detail.

4.3. Control footprint

The set of all control vectors that can be generated by a solar sail is denoted by $\mathcal{B}$, and it is commonly represented with a "bubble" diagram. As an example, Fig. 3a shows a "bubble" viewed from the orbital reference frame $\mathcal{I}$, where the axes u_x, u_y, and u_z indicate the components of the control vector $\boldsymbol{u}$ in $\mathcal{I}$. Note that the bubble is axisymmetric around $\hat{\boldsymbol{S}}$ and always expands away from the sun (the sun is located far towards $-\hat{\boldsymbol{S}}$). The orientation of the bubble in frame $\mathcal{I}$ depends on the relative geometry between $\hat{\boldsymbol{S}}$ and the orbital plane, which is determined by Ω, i, and the current epoch τ. For $\tau = 0$, the geometry displayed in Fig. 3a is obtained for $\Omega = 90$ deg and $i = 140$ deg, which produces $\beta = 50$ deg.

In [26], it was proven that, to obtain an optimal in-plane trajectory, the in-plane projection of the control vector must lie on the contour of the projection of $\mathcal{B}$ onto the orbital plane, referred to as subset $\mathcal{U}_\Pi$ (see the dashed line in Fig. 3a), which is the solar-sail equivalent to the maximum thrust condition when using an ion drive in a minimum-time problem. This condition defines the three-dimensional subset $\mathcal{U} \subset \mathcal{B}$ (see the solid line in Fig. 3a), which is the domain of feasible control vectors.

Because the sun-planet line $\hat{\boldsymbol{S}}$ moves continuously with time, the set $\mathcal{U}$ evolves with time as well, leaving a "footprint" in the orbital plane. Fig. 3b shows the evolution of $\mathcal{U}_\Pi$ in frame $\mathcal{I}$ for $\Delta\tau = 0.28$ and orbit geometry $\Omega = 30$ deg and $i = 60$ deg, where darker colors indicate increasing time. The depicted plane represents the orbital plane. Henceforth, we refer to the evolution of $\mathcal{U}_\Pi$ for a given orbit geometry as the "control footprint". Note that two optimization problems are equivalent only if they have the same control footprint (i.e., the same set of feasible controls). Examples of footprints can be found in Figs. 8 and 13. Moreover, the control footprint provides an idea of the available control during a transfer trajectory; as we explain in Section 5.3, its symmetry can be qualitatively used to explain the characteristics of certain transfers.

4.4. Equivalence ratios

Addressing the equivalence conditions stated in the previous subsections, it is possible to extrapolate transfer performances between planets. For example, consider the planets Earth (subscript $\square_E$) and Mars (subscript $\square_M$) and assume we know the performance of a reference transfer around Earth. The aim is to find the input parameters around Mars that yield the same scaled trajectory, so that we can obtain Δr_M of the Mars transfer as $\Delta r_M = \Delta\rho\, r_{0_M}$, where r_{0_M} is the initial radius around Mars.

Let us assume that the reference transfer around Earth ($\mu_E = 3.986004418 \times 10^5$ km^3/s^2, $P_E = 365.256$ days) starts from a $r_{0_E} = 42{,}164$ km circular orbit with $\Omega = 90$ deg and $i = 60$ deg, has a total transfer time of $\Delta\tau = 0.172$ years, and employs a solar with $a_{0_E} = 0.1$ mm/s^2. With these parameters, the optimized scaled transfer achieves $\Delta\rho = 0.0675$ in 60 orbital revolutions, which corresponds to $\Delta r_E = \Delta\rho\, r_{0_E} = 2{,}846$ km around Earth.

The transfer around Mars ($\mu_M = 4.2828 \times 10^4$ km^3/s^2, $P_M = 686.98$ days) must have the same orbital geometry of $\Omega = 90$ deg and $i = 60$ deg and transfer time of $\Delta\tau = 0.172$ years. Then, from the equivalences $\Sigma_{0_E} = \Sigma_{0_M}$ and $\Psi_{0_E} = \Psi_{0_M}$ we obtain:

$$r_{0_M} = r_{0_E} \sqrt[3]{\left(\frac{P_M}{P_E}\right)^2 \left(\frac{\mu_M}{\mu_E}\right)} \qquad a_{0_M} = a_{0_E} \left(\frac{r_{0_E}}{r_{0_M}}\right)^2 \left(\frac{\mu_M}{\mu_E}\right) \tag{18}$$

Using Eq. (18) with the inputs of the reference trajectory we obtain $r_{0_M} = 30{,}544$ km and $a_{0_M} = 0.021$ mm/s^2. With these values, the scaled problem around Mars is exactly the same as the scaled problem around Earth (i.e., the scaled problem is universal and not planet-dependent). Therefore, we can compute the optimal radius change sought for the Mars transfer as $\Delta r_M = \Delta\rho\, r_{0_M} = 2{,}062$ km.

Table 1 gathers the equivalence ratios for the initial orbit radius and area-to-mass ratio for all planets in the solar system. The values are derived from Eq. (18) but substituting a_0 by A/m via $a_0 = 2p(A/m)$. This substitution is performed because the solar radiation pressure p changes between planets following an inverse square law with heliocentric distance, making a_0 a planet-dependent performance parameter; A/m is therefore a better choice for inter-planet comparisons since it is planet-independent. Hereafter, A/m is used whenever comparisons between planets are presented. Note that, by using the equivalence ratios in Table 1 and following the workflow presented in this subsection, the mission designer can easily obtain equivalent transfers around all planets in the solar system.

There is, however, a fundamental limitation to the equivalence ratios. The perturbative environment (e.g., non-sphericity of the gravity field, third-body effects) of each planet in the solar system is unique. The mission designer must carefully analyze the order of magnitude of these perturbations in the orbital regime under consideration to check if direct extrapolation is possible, especially for long-duration transfers. Note that, if the order of magnitude of the perturbations is similar in the transfer around Earth and the equivalent transfer around the planet

Table 1
Equivalence ratios for all planets in the solar system (inner planets left, outer planets right). The subscript k denotes the corresponding planet in each row.

	r_{0_k}/r_{0_E}	$(A/m)_k/(A/m)_E$		r_{0_k}/r_{0_E}	$(A/m)_k/(A/m)_E$
Mercury	0.15	0.38	Jupiter	35.51	6.82
Venus	0.68	0.93	Saturn	43.70	4.57
Earth	1	1	Uranus	46.77	2.44
Mars	0.72	0.48	Neptune	77.83	2.59

under consideration, the extrapolation would still hold and provide adequate results for a first-order analysis.

5. Best and worst transfer geometry

One can consider a myriad of orbital geometries and initial sun-planet configurations. In this section, we show that it is possible to identify the best and worst initial geometries that yield the best and worst transfer performances, respectively. Using this knowledge, a performance envelope that contains all other geometries can be defined (see Section 6), effectively bounding the problem.

First, the initial phase angle, which is the critical parameter to define the best and worst geometries, is introduced. Then, the concept of the "growth vector" is defined and used to intuitively explain why the best geometry is the best and why the worst geometry is the worst. Finally, we provide a detailed analysis of the control laws required to execute the best and worst transfers.

5.1. Initial phase and aspect angle

The initial phase angle $\zeta_0 = \Omega - \sigma_0$ represents the angle between the line of nodes of the orbit and the sun-planet direction at the initial epoch. Hence, ζ_0 can be varied either by starting the transfer at a different time of the year or by changing the ecliptic RAAN. For simplicity, in this study, we set $\sigma_0 = 0$ (i.e., autumn equinox), but the conclusions drawn in this section still hold for $\sigma_0 \neq 0$. Note that for $\sigma_0 = 0$, $\zeta_0 = \Omega$.

The initial phase angle influences the performance of the MC2C transfers. As an example, Fig. 4a shows the performance $\Delta\rho$ of an MC2C transfer of $\Delta\tau = 0.25$ years in the GEO region ($r_0 = 42{,}164$ km) with an ACS3-like solar sail ($a_0 = 0.05$ mm/s^2) as a function of the initial phase angle ζ_0 for various ecliptic inclinations, where lighter colors indicate smaller inclinations. Each circle represents the performance of an optimized transfer; the colored and numbered solid dots denote specific transfers that are analyzed in detail in the next paragraph. Various important observations can be extracted from Fig. 4a: 1) the best and worst performances are achieved for $i = 90$ deg at $\zeta_{0_b} = \{135, 315\}$ deg and $\zeta_{0_w} = \{45, 225\}$ deg, respectively (i.e., the best and worst cases have a phase offset of ± 90 deg); 2) the effect of ζ_0 decreases with inclination, where at the limit $i = 0$ deg, the initial phase angle has no effect; and 3) the curves are periodic with a period of 180 deg. These trends can be related to the evolution of the aspect angle during the transfer for the various orbital geometries.

To understand the concept of the aspect angle in more detail, Fig. 4b shows the time evolution of the aspect angle β for the five MC2C transfers denoted in Fig. 4a with colored and numbered solid dots. The selected five transfers cover various initial phase angles ($\zeta_0 = \{45, 135, 155, 165\}$ deg) and inclinations ($i = \{0, 60, 90\}$ deg) to show how these parameters influence the evolution of the aspect angle. The aspect angle changes continuously due to the yearly motion of $\hat{\boldsymbol{S}}$ in the ecliptic plane (see Fig. 1a and consult Section IV.B of [19] for further details). The value of β depends on the ecliptic inclination i and the phase angle (i.e., the relative orientation) between the line of nodes of the orbit $\hat{\boldsymbol{l}}$ (inertial) and the sun-planet line $\hat{\boldsymbol{S}}$ (time-dependent): when $\hat{\boldsymbol{S}}$ is parallel to $\hat{\boldsymbol{l}}$, $\beta = 90$ deg because the sun-planet line is contained in the orbital plane (see the red solid line for $\zeta_0 = 45$ deg and $i = 90$ deg in Fig. 4b at the midpoint); whereas when $\hat{\boldsymbol{S}}$ is perpendicular to $\hat{\boldsymbol{l}}$, the minimum aspect angle $\beta_m = \pi/2 - i$ is reached (see black solid and blue dotted lines for $\zeta_0 = 135$ deg in Fig. 4b at the midpoint). Hence, for a given orbital geometry (Ω, i) and a full year, the amplitude of the associated aspect angle curves is $[\beta_m, \pi/2]$. Note that when $i = 0$ deg, the line of nodes is not defined and $\hat{\boldsymbol{S}}$ is always contained in the orbital plane, yielding a constant value for β of 90 deg throughout the year (see horizontal dashed yellow line in Fig. 4b).

According to Fig. 4, the best performance occurs when the minimum aspect angle β_m is reached exactly at the midpoint of the transfer (see how the black solid and blue dotted lines for $\zeta_0 = 135$ deg in Fig. 4b correspond to the best performing cases 2 and 4 in Fig. 4a, respectively), which happens when the sun-planet line $\hat{\boldsymbol{S}}$ is perpendicular to the line of nodes $\hat{\boldsymbol{l}}$ at the midpoint of the transfer [i.e., $\hat{\boldsymbol{S}}(\Delta\tau/2) \perp \hat{\boldsymbol{l}}$]. Conversely, the worst performance occurs when the maximum aspect angle $\beta = 90$ deg is reached at the midpoint of the transfer (see how the red solid line for $\zeta_0 = 45$ deg in Fig. 4b corresponds to the worst performing case 1 in Fig. 4a), which happens when $\hat{\boldsymbol{S}}$ is parallel to $\hat{\boldsymbol{l}}$ at the midpoint of the transfer [i.e., $\hat{\boldsymbol{S}}(\Delta\tau/2) \parallel \hat{\boldsymbol{l}}$]. Hence, for any given transfer time, the best illumination conditions occur when the transfer time is centered around β_m, whereas the worst conditions occur when the transfer time is centered around $\beta = 90$ deg. Note that the best overall illumination conditions occur for $i = 90$ deg when the minimum aspect angle reaches the absolute minimum value of 0 deg at the midpoint of the transfer (i.e., the sun-planet line is perpendicular to the orbital plane at the midpoint of the transfer). In the following two subsections Sections 5.2 and 5.3, we elaborate on the physics behind the relationship between initial sun-plane geometry, aspect angle, and performance.

Although Fig. 4 was generated for a specific transfer time of $\Delta\tau = 0.25$ years, the conclusions drawn from the plots are general. The following relations for the best (ζ_{0_b}) and worst (ζ_{0_w}) initial phases hold true for any transfer time:

$$\zeta_{0_b} = \pi\left(\frac{1}{2} + \Delta\tau\right) \qquad \zeta_{0_w} = \pi\Delta\tau \tag{19}$$

where Eq. (19)-left ensures $\hat{\boldsymbol{S}}(\Delta\tau/2) \perp \hat{\boldsymbol{l}}$, and Eq. (19)-right ensures $\hat{\boldsymbol{S}}(\Delta\tau/2) \parallel \hat{\boldsymbol{l}}$ for any transfer time $\Delta\tau$. Based on Eq. (19), Section 6 computes the performance envelopes for various transfer times.

5.2. Growth vector

To explain the physics behind the best and worst transfer geometries it is useful to introduce the concept of the "growth vector". The growth vector $\boldsymbol{g}$ indicates the direction in which the apogee of the orbit would grow if a pure orbit raising maneuver was executed with the sail. It is defined as $\boldsymbol{g} = \boldsymbol{h} \times \hat{\boldsymbol{S}}$; hence, $\boldsymbol{g}$ is always contained in the orbital plane and perpendicular to the plane formed by $\boldsymbol{h}$ and $\hat{\boldsymbol{S}}$. Fig. 2b contains a schematic of the orbital plane and the vectors involved in the definition of the growth vector. An ellipse is drawn in the orbital plane to represent an already grown orbit, where a sail is shown at various points along the orbit with an appropriate attitude for orbit raising. Making use of a sailing boat analogy, the orbit can be divided into two distinct halves: the downwind half and the upwind half. The division line is given by the projection of the sun-planet line $\hat{\boldsymbol{S}}$ in the orbital plane, denoted by $\boldsymbol{S}_\Pi$. During the downwind half of the orbit, the sailcraft moves away from the sun; the sail is placed mainly perpendicular to the incoming sunlight (the wind) to produce an acceleration along the velocity vector and therefore increase the orbital energy. On the contrary, during the upwind half, the sailcraft moves towards the sun; because no solar-sail acceleration can be generated towards the sun (boats also struggle sailing against the wind) the sail is placed mainly parallel to the incoming sunlight to avoid thrusting opposite to the velocity vector. There is a clear asymmetry in the thrusting profile (i.e., most of the energy is introduced during the downwind half of the orbit), which increases as the aspect angle β increases. For $\beta = 90$ deg, $\hat{\boldsymbol{S}}$ is contained in the orbital plane and the

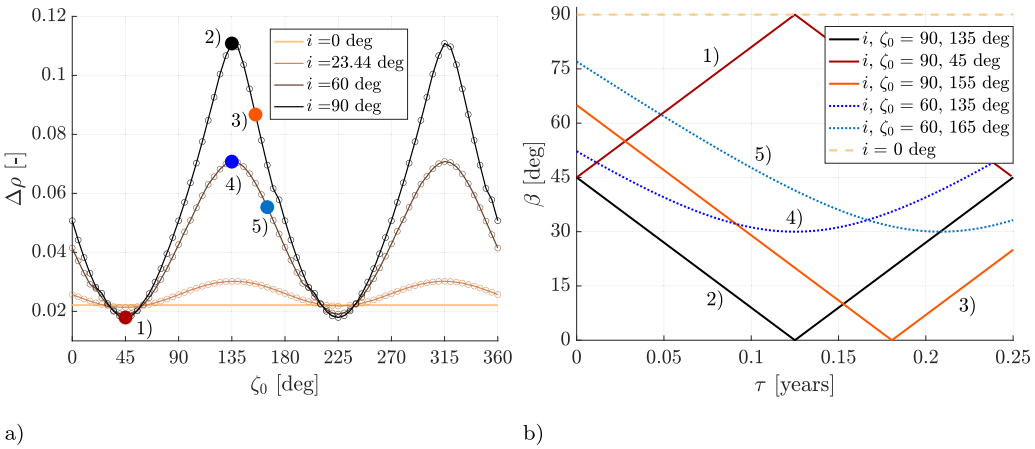


Fig. 4. Relationships between performance $\Delta\rho$, initial phase angle ζ_0, and aspect angle β for an MC2C transfer of $\Delta\tau = 0.25$ years, $a_0 = 0.05$ mm/s^2, and $r_0 = 42{,}164$ km: a) performance as a function of initial phase angle for various ecliptic inclinations; and b) aspect angle evolution for several initial phase angles and inclinations.

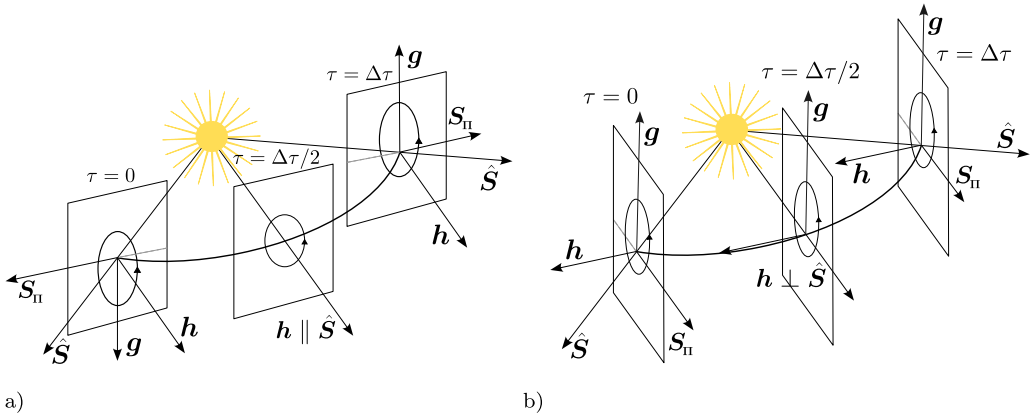


Fig. 5. Schematics of a) best transfer geometry, and b) worst transfer geometry.

asymmetry is maximum (see Fig. 5b at $\tau = \Delta\tau/2$), whereas for $\beta = 0$ deg, there is no asymmetry (see Fig. 5a at $\tau = \Delta\tau/2$); $\beta = 0$ deg is equivalent to a boat sailing on a beam reach. Whenever asymmetry exists, the orbit grows in the direction perpendicular to $\boldsymbol{S}_\Pi$ defined by $\boldsymbol{g}$.

Now that the growth vector has been introduced, we can continue with the explanation of the best and worst transfer geometry. For the remainder of the explanation, we will refer to Figs. 5–7 when needed. Fig. 5 gathers two schematics representing the best and worst transfer geometries. Both schematics depict the planet-centered orbital plane at three epochs: initial ($\tau = 0$), halfway through the transfer ($\tau = \Delta\tau/2$), and final ($\tau = \Delta\tau$). At each epoch, the growth vector $\boldsymbol{g}$ is drawn together with the angular momentum vector $\boldsymbol{h}$ and the sun-planet direction $\hat{\boldsymbol{S}}$. Fig. 6 shows the evolution in orbital revolutions of the eccentricity and the evolution in years of the arguments of the growth (red) and apogee (black) vectors for the best ($\zeta_0 = 135$ deg) and worst ($\zeta_0 = 45$ deg) transfers in Fig. 4a (i.e., the parameters of the transfers are the same as those used to compute Fig. 4a). Note that the argument refers to the angle between an in-plane vector (here, the growth or apogee vectors) and the line of nodes $\hat{\boldsymbol{l}}$. Fig. 7 shows the top view of the same best and worst transfers in the orbital plane. The evolution of the trajectory is represented with the color scale (blue denotes beginning and red end), and the trajectory is scaled from 0.1 to 1 to enable the visualization of the apogee growth.

Let us begin the discussion with the best geometry represented in Figs. 5a, 6a, and 7a. The initial phase is $\zeta_0 = 135$ deg in agreement with Eq. (19)-left for $\Delta\tau = 0.25$, ensuring that at the midpoint, $\hat{\boldsymbol{S}}$ is perpendicular to the line of nodes of the orbit. During the first half of the orbit, the growth vector points opposite to the ecliptic north pole (see the first epoch in Fig. 5a and the argument of the growth vector of 270 deg in 6a), while during the second half, it points along the ecliptic north pole (see the last epoch in Fig. 5a and the argument of the growth vector of 90 deg in 6a). The vector flips exactly at the midpoint (see the red line in 6a). We can see in Figs. 6a and 7a how the eccentricity grows during the first half of the transfer with the apogee aligned with the growth vector (the black and red lines match in Fig. 6a, while it can be appreciated in Fig. 7a how the apogee grows towards the ecliptic south pole). Then, during the second half, the eccentricity decreases as the growth vector points opposite to the apogee. The first half can be understood as the *growth phase* (from blue to yellow in Fig. 7a), whereas the second half as the *circularization phase* (from yellow to red in Fig. 7a). Most importantly, the flip of the growth vector at the midpoint ensures that the orbit circularizes naturally; the optimizer does not have to fight the physics to obtain an MC2C transfer. Indeed, we found that for $i = 90$ deg and $\zeta_0 = \zeta_{0_b}$, no optimization is needed at all; pure propagation following a locally optimal orbit raising maneuver (see [14] for the definition of an orbit raising maneuver) yields an MC2C transfer, because the increase in eccentricity during the growth phase exactly cancels out during the circularization phase. We refer to these elegant transfers as *self-transfers*. If a mission can be accomplished with the particular geometry of the self-transfer, the control law to obtain an MC2C transfer is as simple as a locally optimal orbit raising. Note that for $i < 90$ deg, the self-transfer phenomenon disappears, because the growth vec-

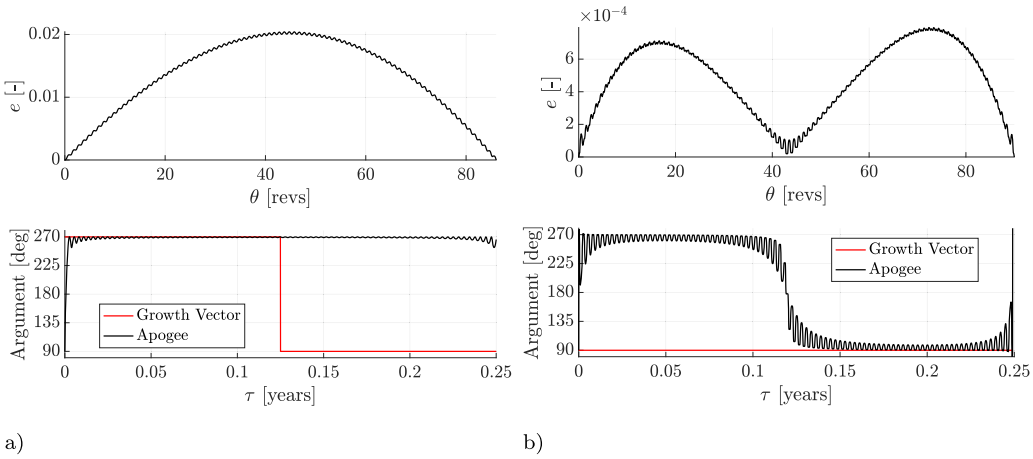


Fig. 6. Evolution of the eccentricity and the arguments of the growth (red) and apogee (black) vectors for an MC2C transfer of $\Delta\tau = 0.25$ years, $a_0 = 0.05$ mm/s^2, $r_0 = 42{,}164$ km, and $i = 90$ deg: a) best transfer geometry ($\zeta_0 = 135$ deg), and b) worst transfer geometry ($\zeta_0 = 45$ deg). (For interpretation of the references to colour in this figure legend, the reader is referred to the web version of this article.)

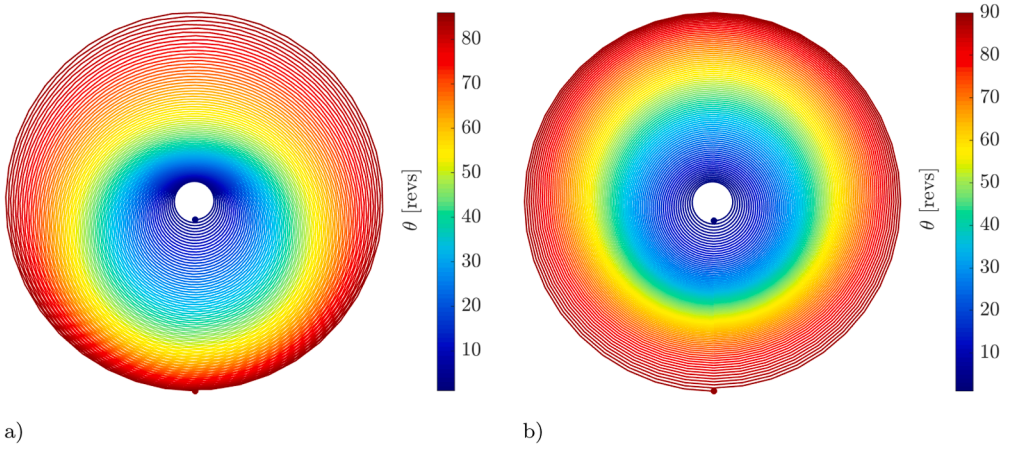


Fig. 7. Top view in the orbital plane of the best (a) and worst (b) transfers. Note that the trajectory is scaled between 0.1 and 1 to ease the visualization of the apogee growth.

tor no longer points in two binary directions but sweeps in the orbital plane.

Let us now consider the worst geometry represented in Figs. 5b, 6b, and 7b. The initial phase is $\zeta_0 = 45$ deg in agreement with Eq. (19)-right for $\Delta\tau = 0.25$, ensuring that at the midpoint, $\hat{\boldsymbol{S}}$ is parallel to the line of nodes of the orbit. Opposite to the best geometry, in the worst geometry, the growth vector is aligned with the ecliptic north pole during the whole transfer (see all epochs in Fig. 5b and the argument of the growth vector of 90 deg in Fig. 6b). As a consequence, the optimizer needs to find a complex control law that manages to increase the orbital radius (i.e., orbital energy) while keeping the eccentricity in check. In other words, the optimizer needs to fight the natural dynamics, which would rather prefer the eccentricity to grow indefinitely. We can see in Fig. 7b and the eccentricity evolution in Fig. 6b the presence of two distinct growth and circularization phases. We refer to this distinct pattern in the eccentricity evolution as *eccentricity reversals*.

To properly understand the eccentricity reversals, it is important to consider the following two points related to the alignment of the growth vector and the apogee: 1) if the growth vector and apogee are aligned, it is natural for the eccentricity to grow (i.e., growth phase); and 2) if they oppose each other, it is natural for the eccentricity to decrease (i.e., circularization phase). Now focus on the argument of the growth vector in Fig. 6b: during the first and last quarters of the transfer, the apogee grows and decreases opposite to and aligned with the growth vector, respectively (i.e., sub-optimal maneuvers against the natural dynamics); conversely, during the second and third quarters, the situation reverses, ensuring optimal maneuvers that exploit the natural dynamics. In a nutshell, the optimizer tries to have the longest possible fraction of optimal maneuvering during the transfer. To accomplish that, it is forced to reach a compromise solution, where sub-optimal segments are placed at the beginning and end of the transfer. The sub-optimality of the worst case versus the better performance of the best case can be easily appreciated in the computed optimal control, which is analyzed in detail in the next subsection (Section 5.3).

5.3. Control

The control strategy to achieve an MC2C transfer heavily depends on the initial phase and inclination of the orbital plane. In this subsection, we analyze in detail the computed optimal control for the best and worst transfers in Fig. 4a, which are completely different.

The most intuitive way to show such differences is to plot the control footprints for both geometries (consult Section 4.3 for a detailed explanation of the control footprint). Fig. 8 shows the control footprints for the best and worst transfers in Fig. 4a (the parameters of the transfers are those used to compute Fig. 4a), where the time evolution of the control is indicated from light to dark colors, respectively. The lines de-

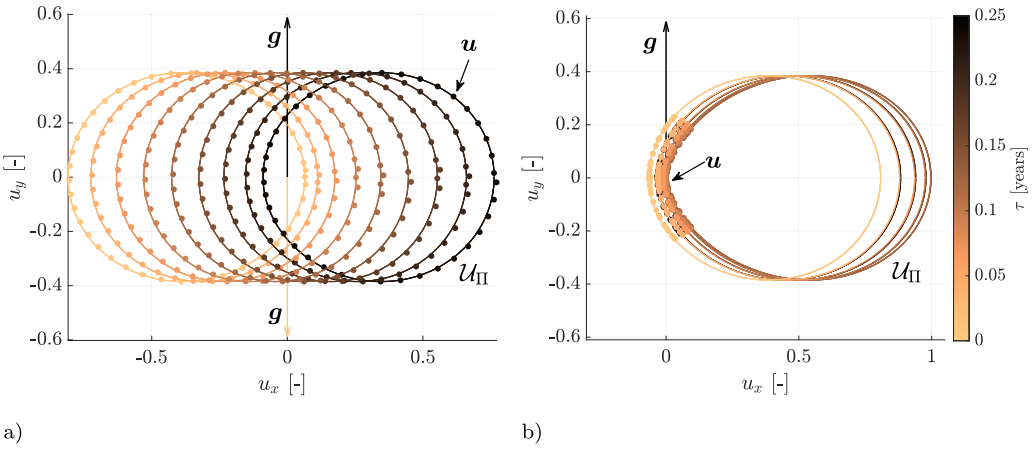


Fig. 8. Control footprints for the best (a) and worst (b) transfers. The lines denote $\mathcal{U}_\Pi$, the solid circular markers represent the optimal $\boldsymbol{u}$, and the arrows the growth vector $\boldsymbol{g}$.

note the projection of the set of feasible controls $\mathcal{U}$ in the orbital plane, $\mathcal{U}_\Pi$. The solid circular markers represent the computed optimal control. The growth vector is added for reference. The first difference that strikes the eye is the misuse of control in the worst case: the computed optimal control clusters around the origin, never accessing the full set of feasible controls. Secondly, the footprint is symmetric with respect to both axes in the best case (see Fig. 8a), whereas in the worst case the footprint is only symmetric with respect to the u_x-axis (see Fig. 8b). The asymmetry can be linked to the misuse of control and the growth vector. In our experience, symmetric footprints allow for full usage of the footprint, whereas asymmetric footprints lead to control misuse. Moreover, symmetric footprints arise when the growth vector opposes itself at some epoch throughout the transfer, whereas asymmetric footprints are typical when the growth vector points in the same direction throughout the transfer.

Fig. 9 shows the computed primer vectors and corresponding control vectors at the midpoint of the best and worst transfers in Fig. 4a for one orbital revolution. Because the shown revolution is at the midpoint of the transfer, the sun-planet line $\hat{\boldsymbol{S}}$ is perpendicular to the page in Fig. 9a (i.e., $\beta = 0$ deg), whereas in Fig. 9b the sun is located towards the left of the page (i.e., $\beta = 90$ deg). It is relevant to note that although only one revolution is shown in Fig. 9, the displayed patterns are a good representation of the entire transfer. The situation in Fig. 9a resembles what one would expect when using an ion drive: the primer and control vectors are mostly aligned with the direction of the velocity vector, leading to a somewhat homogeneous energy intake during the whole revolution. In stark contrast, the primer vectors in Fig. 9b point mainly towards the sun, which poses a complex challenge for solar-sail propulsion. Recall that the primer vector represents the optimal thrusting direction in which the projection of the solar-sail acceleration has to be maximized. The part of the bubble that can produce acceleration along the primers in Fig. 9b is the region around the origin, which is what we see in Fig. 8b. This behavior of the primer vector is linked to the aspect angle and was identified for the first time in [26] when characterizing one-revolution transfers. In particular, [26] details that, when $\beta \approx 0$ deg, the primer vector oscillates around the velocity vector; as β increases, a regime change occurs and the primer vector starts oscillating around the projection of the sun-planet line in the orbital plane $\boldsymbol{S}_\Pi$ (see the definitions of the *ion-drive regime* and *solar-sail regime* in [26] for more details).

Finally, Fig. 10 presents the evolution of the cone angle α for the best and worst transfers in Fig. 4a. The dashed and dotted lines mark the maximum and minimum cone angles of the set of feasible controls, respectively (i.e., the maximum and minimum cone angles of the footprint in Fig. 8, respectively; see [26] for more details). For the best case in Fig. 10a, the cone angle (solid line) reaches the maximum and minimum cone angles, indicating that the set of feasible controls is being fully used (see Fig. 8a for an intuitive visualization). Note how, exactly at the middle of the transfer, the maximum and minimum lines intersect at the value 35.26 deg. At the midpoint of the transfer, the primer vector is contained in a plane perpendicular to $\hat{\boldsymbol{S}}$ (i.e., $\beta = 0$ deg, Fig. 9a); it is known that, to maximize the solar-sail acceleration in any direction perpendicular to $\hat{\boldsymbol{S}}$, a cone angle of 35.26 deg is optimal [14].

The control misuse in the worst case can be clearly seen in Fig. 10b: the black continuous line never reaches the limit $\alpha_{\min}$, implying that the set of feasible controls is not being used to its maximum extent (see Fig. 8b for an intuitive visualization). Note how, due to the worst geometry condition, exactly at the middle of the transfer, the sun-planet line is contained in the orbital plane ($\beta = 90$ deg, Fig. 9b) and therefore the minimum and maximum cone angles are 0 and 90 deg. In addition, note the large values of the cone angle that are needed to transfer in the worst case ($\alpha > 50$ deg in Fig. 10b); at such high values of the cone angle, the solar-sail acceleration is hard to predict and control [14,16]. Indeed, when considering more complex acceleration models (e.g., optical model, parametric model), the maximum achievable cone angle is smaller than 90 deg [21]. Hence, it is probable that transfers close to the worst geometry become unfeasible under higher-fidelity dynamics. A corollary of the latter observation is that it is wise to first optimize transfers with the ideal solar-sail model, so that one can identify unfeasible transfers under higher-fidelity solar-sail acceleration models.

The main conclusion of the previous subsection (Section 5.2) and this subsection can be summarized as follows. The more propitious geometry of the best transfer ensures natural growth and circularization phases, which allows for better usage of the available control and therefore yields better performance. On the contrary, the cumbersome geometry of the worst transfer challenges the optimizer to find a delicate balance between energy intake and eccentricity control, which results in a poor usage of the available control and therefore lower performance.

6. Performance envelopes

The performance envelopes are plots of transfer time $\Delta\tau$ versus performance $\Delta\rho$. They provide estimates of the best and worst transfer times for a given target radius increase $\Delta\rho$ and vice versa. By using the performance envelopes, the mission designer can easily assess the performance of various MC2C transfers without computing them; an ideal tool for early mission design, when hundreds of trajectories need to be considered and estimated values suffice.

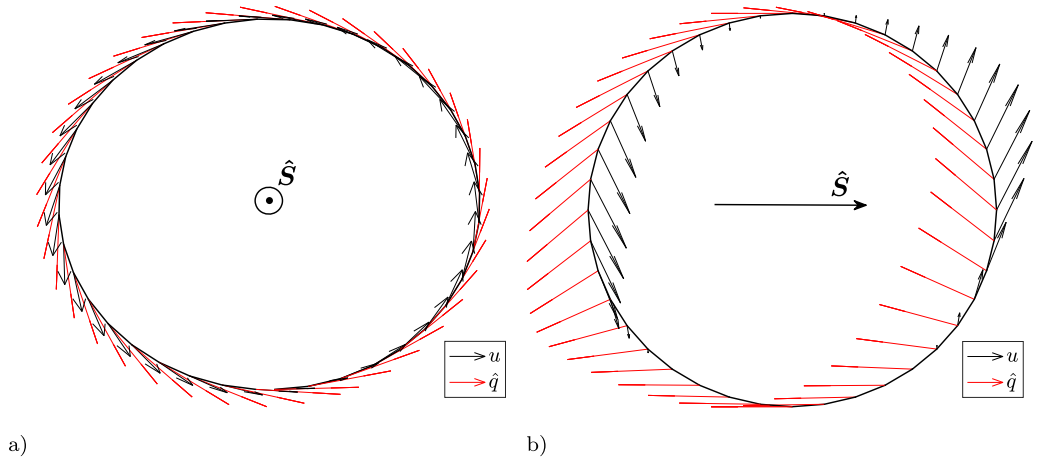


Fig. 9. Primer vectors and corresponding control vectors at the midpoint of the best (a) and worst (b) transfers for one orbital revolution.

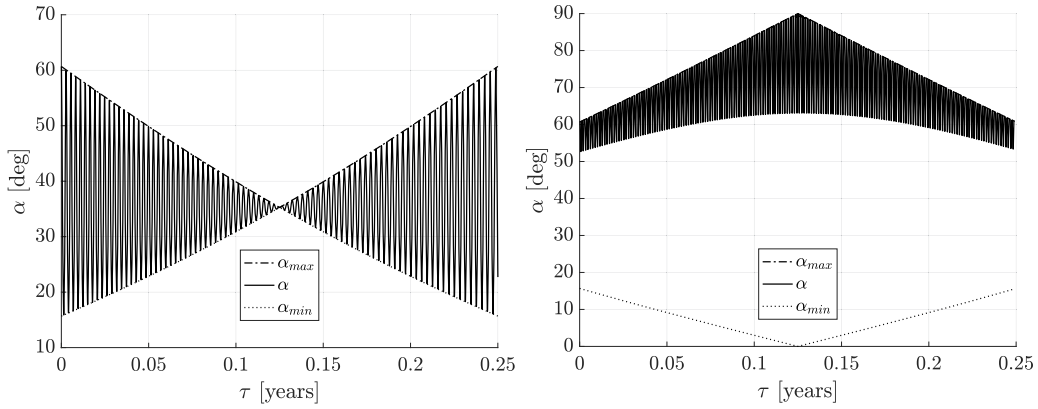


Fig. 10. Evolution of the cone angle for the best (a) and worst (b) transfers. The dashed and dotted lines mark the maximum and minimum cone angles of $\mathcal{V}$, respectively.

6.1. One-year envelopes

Fig. 11 shows the one-year ascent (subplot a) and descent (subplot b) performance envelopes for an ACS3-like solar sail with $a_0 = 0.05$ mm/s^2 in the GEO region ($r_0 = 42{,}164$ km) for various ecliptic inclinations, where lighter colors indicate decreasing inclination. The solid lines indicate the best case (i.e., best initial phase ζ_{0_b} according to Eq. (19)-left), whereas the dashed lines represent the worst case (i.e., worst initial phase ζ_{0_w} according to Eq. (19)-right). The best/worst lines "envelop" a region in the $(\Delta\tau, \Delta\rho)$-plane that contains all possible initial phases in between $[\zeta_{0_w}, \zeta_{0_b}]$. In other words, for a given target $\Delta\rho$, a transfer with phase ζ_0 in between $[\zeta_{0_w}, \zeta_{0_b}]$ would yield a transfer time in between $[\Delta\tau_b, \Delta\tau_w]$.

The width of the envelope is the difference between the best and worst lines. The envelopes in Fig. 11 widen as the transfer time approaches 0.5 years, narrowing afterwards, until all lines intersect the solid black line at approximately one year. The widest envelope corresponds to an ecliptic inclination of 90 deg (see how the black lines engulf all other lines in Fig. 11). As inclination decreases, the maximum width of the envelopes decreases, until $i = 0$ deg, where there is no "envelope": the best and worst lines coalesce in one single line (the red line for $i = 0$ deg in Fig. 11). Recall from Fig. 4 that the initial phase has no effect when $i = 0$ deg, effectively removing the distinction between best and worst initial phase angle.

Finally, for a given $\Delta\tau$, the achieved $\Delta\rho$ is larger when ascending than when descending (see how the curves in Fig. 11a reach larger values of $\Delta\rho$ than those in Fig. 11b for any $\Delta\tau$). The gravitational well becomes steeper the closer to the planet, making it harder to descend than to ascend.

6.2. Periodicity of the envelope

Fig. 12 presents the extension up to two years of Fig. 11a. The horizontal axis is no longer shown in logarithmic scale as in Fig. 11 to enhance the features around one year. In addition, Fig. 12b provides a zoomed view around one year. The envelopes seem to have a periodic nature, matching the one-year periodic evolution of the aspect angle. All envelopes "close" at the one-year mark (see how the best/worst lines merge at $\Delta\tau = 1$ year in Fig. 12b), re-opening again as transfer time increases further.

It is interesting to see how the envelopes for smaller inclinations become better (i.e., less $\Delta\tau$ for a given $\Delta\rho$) than the envelop for the best case of $i = 90$ deg (black line) around the one year mark. Fig. 12b clearly shows how the smaller inclination envelopes "overtake" the black $i = 90$ deg envelope around 0.85 years. However, the phenomena is reversed some time later around 1.2 years, when the envelopes for the smaller inclinations once again fall back inside the black envelope. Fig. 12a seems to indicate that this "bump" is periodic, where the size of the bump appears to increase every year (see how the lighter envelopes overtake the black envelope earlier around 1.7 years in Fig. 12a). With each year that passes, the lighter smaller inclination envelopes seem to become better and better, approaching the solid black line and thus increasing the size

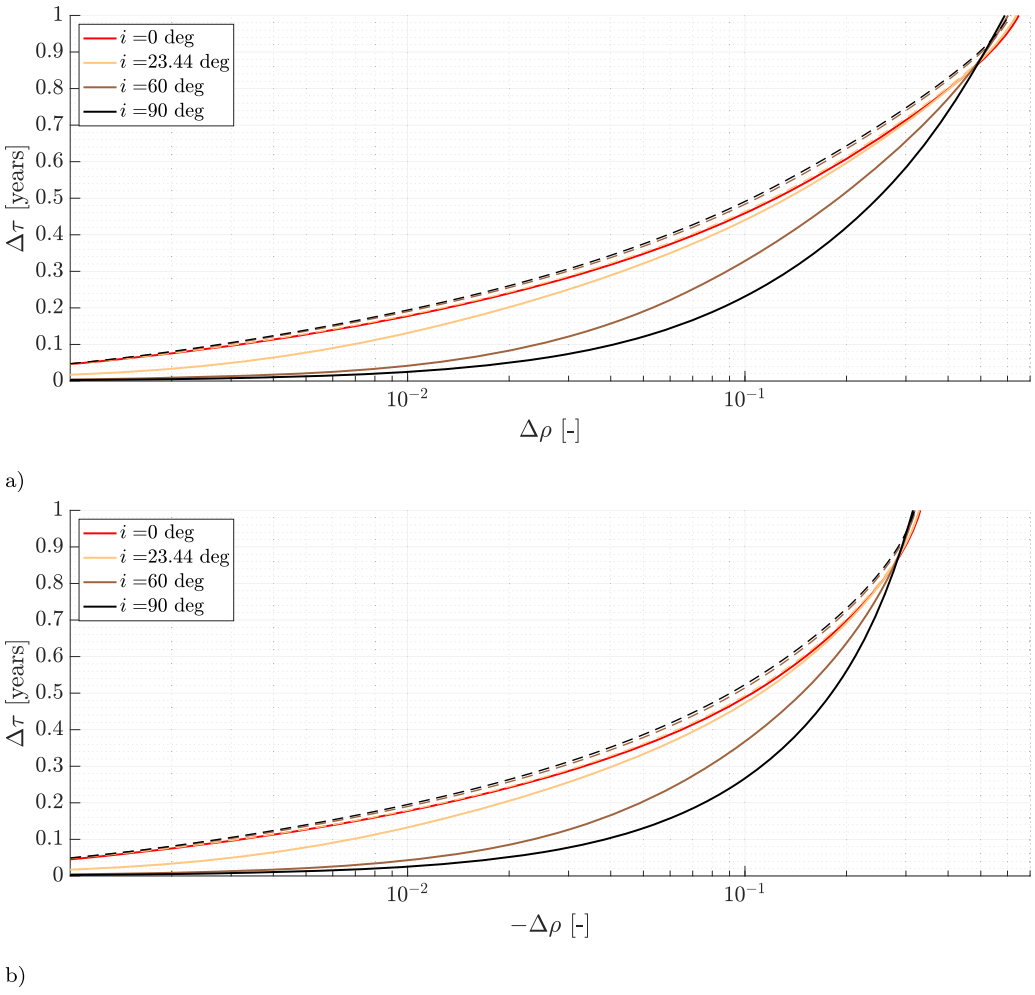


Fig. 11. One-year ascent (a) and descent (b) performance envelopes for an ACS3-like sail ($a_0 = 0.05$ mm/s^2) in GEO ($r_0 = 42{,}164$ km). $\Gamma_0 = 0.51$.

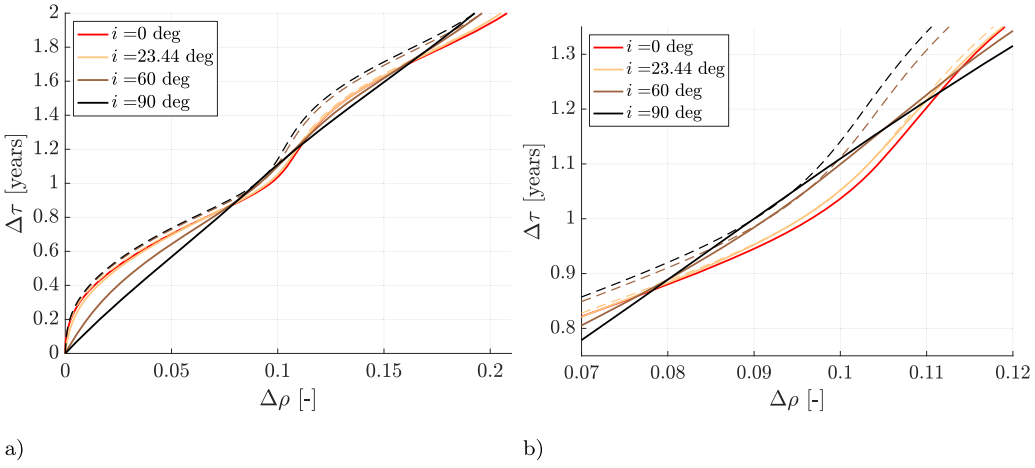


Fig. 12. Extension up to two years of the one-year ascent envelope, where b) is a zoomed image of a) around one year.

of the bump. Longer envelopes would be needed to fully validate this hypothesis, but such long MC2C transfers are impractical in reality.

The presence of the bump and the performance enhancement of the smaller inclination envelopes can be physically explained by looking at the control footprints and the evolution of the growth vector. Fig. 13 shows the control footprint (lines) together with the optimal control (dots) and the growth vector (arrows) for two MC2C transfers of different transfer times (0.43 and 1 years). The inclination is $i = 0$ deg (the red line in Figs. 11 and 12), which causes the growth vector to continuously rotate in the orbital plane with a 90 deg phase offset with respect to $\hat{\boldsymbol{S}}$.

What we can observe from Fig. 13 is the behavioral change of the optimal control when the transfer time is long enough. Up to a critical value for the transfer time (i.e., around 0.75 years in this example), the optimal control does not populate the full footprint (see Fig. 13a), while after that critical value, it does (see Fig. 13b). A fully populated

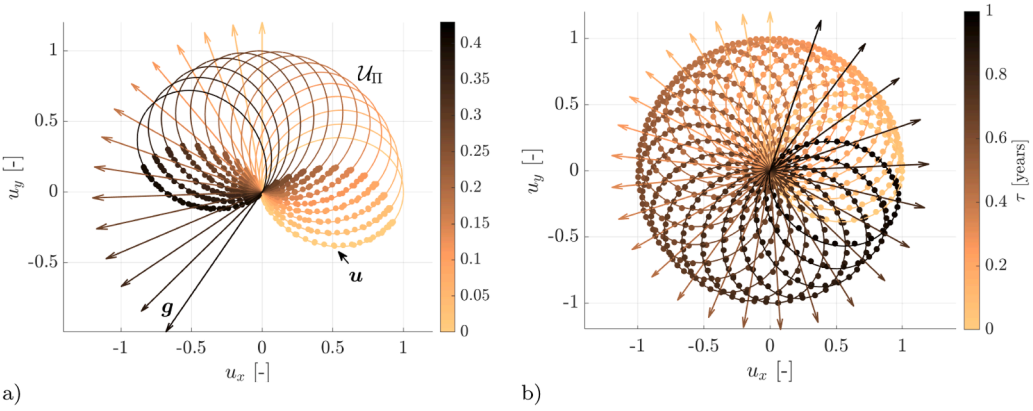


Fig. 13. Control footprint (lines), optimal control (dots), and growth vector (arrows) for two $i = 0$ deg MC2C transfers of different transfer times: a) $\Delta\tau = 0.43$ years, b) $\Delta\tau = 1$ year.

footprint implies better usage of the available control and larger control magnitudes, which explains the increase in performance of the smaller inclination envelopes for transfer times beyond one year.

We believe that the behavioral change observed in Fig. 13 is related to the continuous evolution of the growth vector. In this example, the growth vector rotates counter-clockwise in the orbital plane. If the growth vector rotates enough (i.e., around 270 deg in this example), the optimizer allows the control to fully use the control footprint, because the eccentricity growth caused during the first half of the transfer can be efficiently counteracted during the second half (i.e., the growth vector points in the opposite direction during the second half of the transfer, similarly to a self-transfer).

7. Extrapolation method

The envelopes presented in Section 6 are computed for one specific sail with $a_0 = 0.05$ mm/s^2 at a radius of $r_0 = 42{,}164$ km around Earth. In theory, if one changes the radius, the performance of the sail, or the planet, Fig. 11 is no longer applicable. In this section, we investigate the possibility of extrapolating Fig. 11 to other radii, sail performances, and planets.

7.1. Equivalent trajectories

Let us introduce the new scaled parameter $\Gamma_0 = \Sigma_0\Psi_0$. It appears that two trajectories with the same geometry and the same value for Γ_0 yield almost the same $\Delta\rho$, despite having different values for r_0 and a_0. Fig. 14 shows the scaled perigee ρ_p as a function of the apogee ρ_a of two $\Delta\tau = 1$ year MC2C transfers around Earth with $\Omega = 0$ deg, $i = 60$ deg, and $\Gamma_0 = 0.51$. The first trajectory (red) has an initial radius of $r_0 = 8{,}378$ km and $a_0 = 0.1122$ mm/s^2, whereas the second trajectory (black) uses $r_0 = 206{,}378$ km and $a_0 = 0.0226$ mm/s^2. Although the trajectories occur in two completely different orbital regimes (i.e., LEO and well beyond GEO), one can see that their resulting performances are almost the same ($\Delta\rho \approx 0.6$). Moreover, the average structure of both transfers is remarkably alike. In other words, if one overlooks the periodic oscillations, the evolution of the eccentricity is quite similar.

Fig. 15 shows the scaled trajectory plot for the two transfers of Fig. 14. One can see that, although having a very different number of orbital revolutions (i.e., 2988 vs 25), the structure of the transfer looks alike. In both cases, the counterclockwise rotation of the growth vector in the orbital plane induces a counterclockwise rotation in the direction in which the apogee growths. Note the similarity in the colored regions, which indicates similar apogee evolution.

The two trajectories in Figs. 14 and 15 have different altitudes, which yield different values for Σ_0. The transfer starting from a lower altitude (subscript $\square_L$) has $\Sigma_{0_L} = 25{,}982$, whereas the transfer starting from a

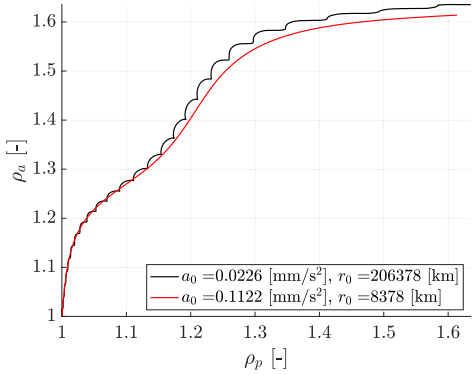


Fig. 14. Scaled perigee-apogee plot of two $\Delta\tau = 1$ year MC2C transfers around Earth with $\Omega = 0$ deg, $i = 60$ deg, and $\Gamma_0 = 0.51$.

higher altitude (subscript $\square_H$) has $\Sigma_{0_H} = 213$. To keep Γ_0 constant, Ψ_0 must change inversely, yielding: $\Psi_{0_L} = 1.98 \times 10^{-5} < \Psi_{0_H} = 2.41 \times 10^{-3}$. Recall from Eq. (16) that, for a given $\Delta\tau$, larger Σ_0 gives the control more orbital revolutions to influence the trajectory and thus increase the final $\Delta\rho$. Moreover, larger values of Ψ_0 also give the control more authority to increase $\Delta\rho$. Therefore, if we want two trajectories at different altitudes to yield the same $\Delta\rho$, it makes sense that $\Psi_{0_L} < \Psi_{0_H}$. Indeed, for the transfer starting from a lower altitude, the increase in $\Delta\rho$ due to the larger number of revolutions is compensated by the lower control authority and vice versa. In summary, the new parameter Γ_0 represents the combined effect of both Σ_0 and Ψ_0, where it appears that for a given $\Delta\tau$, two MC2C transfers with the same orbital geometry and Γ_0 produce the same $\Delta\rho$ with the same transfer structure.

Substituting the definitions of Σ_0 and Ψ_0 into $\Gamma_0 = \Sigma_0\Psi_0$, we find $\Gamma_0 = a_0 P\sqrt{r_0/\mu}$. This expression indicates that Γ_0 is proportional to both a_0 and r_0, but that it is more sensitive to changes in a_0 (i.e., $\Gamma_0 \propto a_0$ versus $\Gamma_0 \propto \sqrt{r_0}$). Fig. 16a shows various lines for constant Γ_0 in the (a_0, r_0)-plane for Earth, where lighter colors indicate decreasing values of Γ_0. The light green line corresponds to $\Gamma_0 = 0.51$, which is the value for the envelopes in Fig. 11 and the reference value in Section 7.2. The horizontal dotted lines are placed at current ($A/m = 5.5$ m^2/kg, $a_0 = 0.05$ mm/s^2 at Earth), near-term ($A/m = 11$ m^2/kg, $a_0 = 0.1$ mm/s^2 at Earth), and future ($A/m = 110$ m^2/kg, $a_0 = 1$ mm/s^2 at Earth) values of the characteristic acceleration [1]. The vertical dashed lines mark the radius of the LEO (7,178 km), medium Earth orbit (MEO) (21,378 km), and GEO (42,164 km) orbital regions. The horizontal axis is expressed in Earth radii.

If a_0 and r_0 are changed such that one moves along a line for constant Γ_0, the associated MC2C trajectories have the same structure and

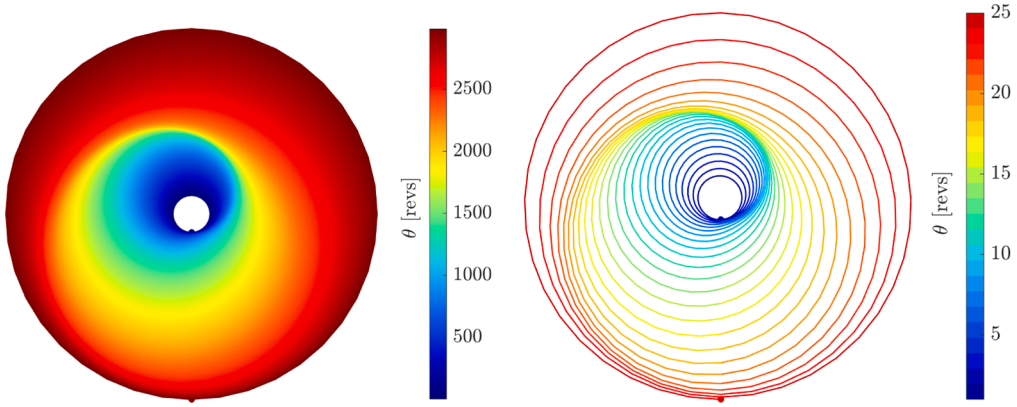


Fig. 15. Scaled trajectories of two $\Delta\tau = 1$ year MC2C transfers around Earth with $\Omega = 0$ deg, $i = 60$ deg, and $\Gamma_0 = 0.51$: a) 2988 revs, and b) 25 revs.

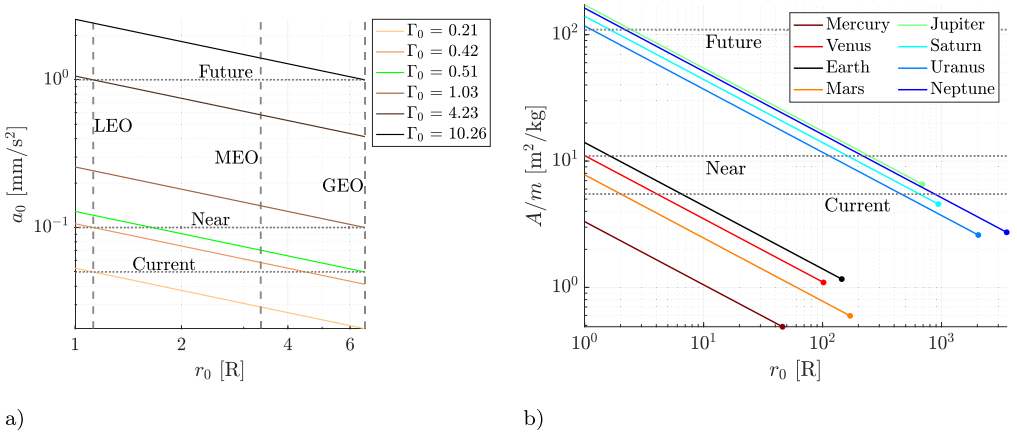


Fig. 16. Lines with constant values of Γ_0: a) various values of Γ_0 for combinations of characteristic acceleration and initial radius around Earth; b) only $\Gamma_0 = 0.51$ (as used for Fig. 11) for combinations of area-to-mass ratio and initial radius for all planets.

performance. Hence, the envelopes in Fig. 11 are directly applicable to all combinations of a_0 and r_0 in Fig. 16a that yield $\Gamma_0 = 0.51$. For example, current sail technology at GEO altitude and near-term technology in between LEO and MEO both lead to $\Gamma_0 = 0.51$ (see intersections in Fig. 16a), so even for different technology and orbital region, Fig. 11 can be used.

It is possible to compute the combinations of a_0 and r_0 that yield $\Gamma_0 = 0.51$ for all planets in the solar system to find out where the envelopes in Fig. 11 apply for each planet. Fig. 16b shows lines of constant $\Gamma_0 = 0.51$ for combinations of area-to-mass ratio A/m in m^2/kg and initial radius in planet radii R. Similar to Fig. 16a, three horizontal dotted lines mark current, near-term, and future sail technology. The lines of constant $\Gamma_0 = 0.51$ start on the vertical axis at the surfaces of the planets ($r_0 = 1\ R$) and end at the planets' spheres of influence (solid circular markers). The bluish colors represent the outer gaseous planets, while the reddish represent the inner rocky planets; the Earth is denoted in black. There is a considerable range of values for r_0 in between the "Current" and "Near" horizontal lines for Earth, Venus, and Mars: Fig. 11 could be directly applied to analyze near-term missions around these planets. Conversely, to use Fig. 11 for transfers around the outer gaseous planets, one would need to consider futuristic sails. Finally, Fig. 11 cannot be immediately applied for Mercury with current sail technology; to use the figure, one would need to downgrade the performance of current sails or find a method to extrapolate Fig. 11 to other values of Γ_0.

7.2. Extrapolation error characterization

In the previous subsection, we discussed how Fig. 11 can be directly applied to parameter combinations that yield $\Gamma_0 = 0.51$. The next question arises: how to extrapolate the envelopes in Fig. 11 to other values of Γ_0. To answer the question, we propose the following extrapolation method:

$$\Delta\rho(\Delta\tau) = \eta(\Delta\tau)\,\frac{\Gamma_0}{G_0} \tag{20}$$

where $\eta(\Delta\tau) : \mathbb{R} \to \mathbb{R}$ is a reference performance curve (e.g., a line in Fig. 11a) and G_0 is its associated reference value of the parameter Γ_0. Eq. (20) represents a simple proportionality relation between the performances of two equally long MC2C transfers with the same orbital geometry but with different values of Γ_0. Note that if the value of Γ_0 is the same, the performance of both transfers is the same and equal to the reference performance η.

Eq. (20) is an approximated extrapolation method. To characterize the extrapolation error, we compute various performance curves (i.e., $\Delta\rho(\Delta\tau)$) for several different values of Γ_0. Then, we obtain the inverse reference performances as:

$$\eta_i = \frac{\Delta\rho}{\Gamma_0/G_0} \tag{21}$$

Because the extrapolation is not perfect, the inverse reference performance η_i differs from the reference performance η. Hence, we can write

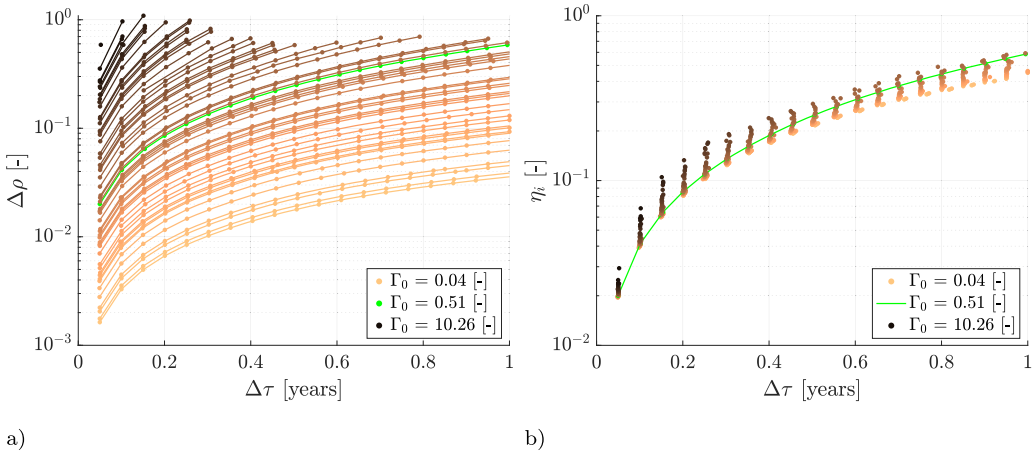


Fig. 17. Performance (a) and inverse reference performance (b) curves for various values of the parameter Γ_0. Best ascent case.

the relative extrapolation error as:

$$\varepsilon_\eta = \frac{|\eta_i| - |\eta|}{|\eta|} \tag{22}$$

where $|\square|$ denotes the absolute value. The absolute values are needed to account for descent trajectories. Note that when $\varepsilon_\eta > 0$, $|\eta| < |\eta_i|$ and the method underestimates the real performance. Conversely, when $\varepsilon_\eta < 0$, $|\eta| > |\eta_i|$ and the method overestimates the real performance.

Fig. 17a shows many different performance curves for various values of Γ_0, where lighter colors indicate smaller Γ_0. The light green curve is the reference performance curve for the best ascent case (i.e., the solid black line in Fig. 11a). All other curves are computed with the same geometry (i.e., $i = 90$ deg, and $\Omega = \zeta_{0_b}$ derived from Eq. (19)-left) but with different initial radii around Earth and with different characteristic accelerations to yield different values of Γ_0. More precisely, the considered values for r_0 and a_0 are $r_0 = \{7{,}178,\ 8{,}378,\ 11{,}378,\ 13{,}378,\ 21{,}378,\ 31{,}378,\ 42{,}164,\ 56{,}378,\ 106{,}378\}$ km and $a_0 = \{0.01,\ 0.025,\ 0.05,\ 0.1,\ 0.25,\ 0.5,\ 1.0\}$ mm/s^2, respectively. By combining these sets, a wide range of values for Γ_0 is achieved, where the minimum and maximum values are 0.04 and 16.3, respectively. To cover transfer times that exceed one year, the transfer time is varied from 0.05 to 1.2 years in 0.05 increments. Each dot in Fig. 17a represents a successfully converged MC2C transfer.

We can infer from Fig. 17a that performance increases with Γ_0, which agrees with the idea that Γ_0 represents the influence of the control on the trajectory. More importantly, all curves seem to scale proportional to Γ_0 without changing shape; only the curves for the largest values of Γ_0 appear to become steeper than the rest. In addition, one can see that for large values of Γ_0, the performance curves end abruptly before reaching a transfer time of 1 year. In fact, the larger Γ_0, the earlier the curves end. What happens is that, in some cases, the influence of the control is large enough to enable the sailcraft to escape the planet mid-transfer, causing the optimization algorithm to diverge. There is a limit on the value of Γ_0 that depends on $\Delta\tau$, because the longer the transfer, the more probable it is that the sailcraft reaches escape conditions. Note that the largest value of Γ_0 that produced a converged trajectory was 10.26, which corresponds to a 0.052 years (14 revs) MC2C transfer with $a_0 = 1$ mm/s^2, $r_0 = 42{,}164$ km, $i = 90$ deg, and $\Omega = 99$ deg.

Fig. 17b presents the computed inverse reference performances (Eq. (21)) of the optimized transfers (dots) in Fig. 17a. Again, the light green curve denotes the reference performance curve of the best ascent case. The agreement between the values η_i and the curve $\eta(\Delta\tau)$ is remarkable, considering that we tested a range of Γ_0 that spans four orders of magnitude. These results show the validity of the proposed extrapolation method in Eq. (20). Nonetheless, the dispersion of the values η_i around the curve $\eta(\Delta\tau)$ points out a non-negligible extrapolation error, which has to be characterized.

Fig. 18 shows two views of the computed relative extrapolation error ε_η associated with Fig. 17. Fig. 18a is the three-dimensional view and Fig. 18b is the side view, where $\Delta\tau$ and Γ_0 constitute the horizontal plane, while ε_η is displayed along the vertical axis. The light green plane marks the value of G_0 of the reference performance curve. Lighter colors denote decreasing Γ_0. The limits of the vertical axis are set to $[-28\%, 66\%]$ for better visualization; the error for the darkest curves reaches up to 600%. From Fig. 18, it is clear that the relative extrapolation error grows in two ways: 1) when transfer time grows, and 2) when Γ_0 differs more from G_0. We can see that, when $\Gamma_0 > G_0$, the error is positive and explodes rapidly (see how the darker lines in Fig. 18b have a much larger slope than the lighter lines). Conversely, when $\Gamma_0 < G_0$, the error is negative and remains within reasonable levels for much longer (see in Fig. 18a how the lighter part to the left of the green plane remains bounded by -25% throughout the year).

As mentioned, positive error indicates that the method underestimates the real performance. When $\Gamma_0 > G_0$, the influence of the control increases with respect to the reference, causing the performance curves to change shape and increase in magnitude (see how the darker performance curves in Fig. 17a become steeper). Eq. (20) successfully captures most of the change in magnitude. Hence, the error displayed in Fig. 18 is mainly due to the change in shape. To explain the change in shape, let us recall the scaled EOMs (Eq. (16)) and point out that the gravitational term is of order $\mathcal{O}(1/\rho^2)$. The larger the input $\Delta\tau$ and Γ_0, the larger ρ becomes during the transfer. As ρ increases, the gravitational term becomes smaller and smaller, indirectly increasing the influence of the control over the whole transfer. The extrapolation error appears because Eq. (20) only accounts for the direct effect of increasing Γ_0, but not for the indirect effect caused by larger ρ. Following the same logic, one can conclude that when $\Gamma_0 < G_0$, the error becomes negative, which is what we observe in Fig. 18.

Although Fig. 18 is useful to understand the trends of the relative extrapolation error, it does not clearly show the boundaries. To solve the issue, Fig. 19 presents contours of constant ε_η in the $(\Gamma_0, \Delta\tau)$-plane, where lighter colors indicate decreasing error. The red line shows the maximum achieved $\Delta\tau$ before escape, and the light green line marks G_0. Fig. 19 can be understood as the domain of the extrapolation method when using as reference performance curves the envelopes in Fig. 11 (i.e., the extrapolation method could be used with any reference G_0, but the error analysis would have to be repeated for that G_0). Given a pair of values Γ_0 and $\Delta\tau$ associated with an MC2C transfer, one can enter Fig. 19 to find a conservative estimate of the extrapolation error, which can be used to adjust the results obtained with Eq. (20) (see the examples in Section 7.3).

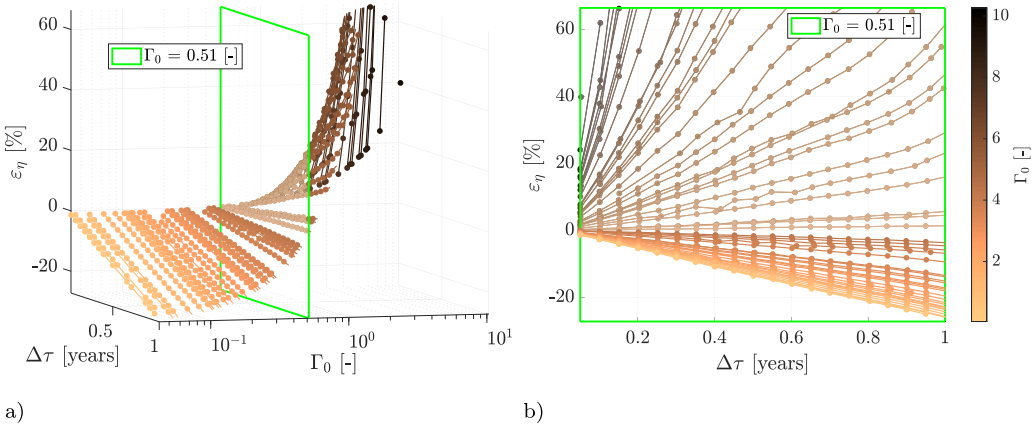


Fig. 18. Relative extrapolation error ε_η for the best ascent case: a) three-dimensional view, and b) side view.

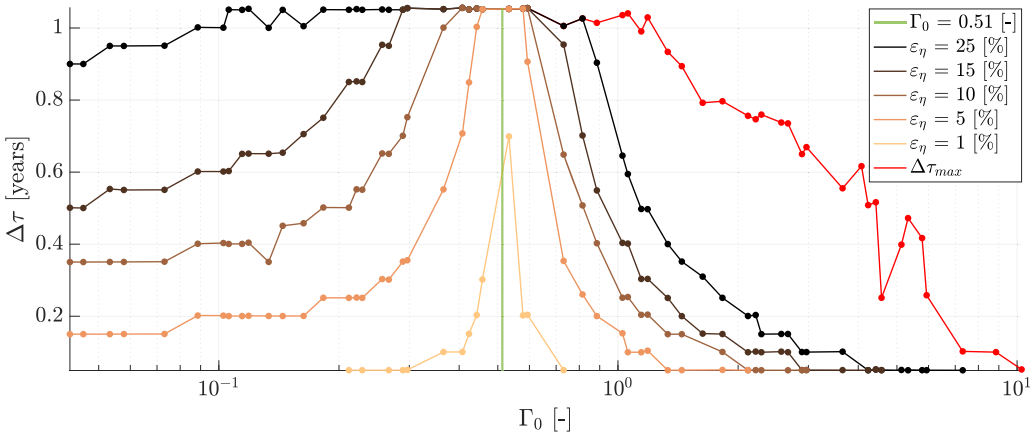


Fig. 19. Contours of constant relative extrapolation error for the best ascent case. The red line shows the maximum achieved transfer time before escape. (For interpretation of the references to colour in this figure legend, the reader is referred to the web version of this article.)

To link Fig. 19 with transfers around Earth we can examine Fig. 16a. From the figure one can extract that for initial altitudes in between LEO and GEO, $\Gamma_0 \in [0.42, 1.03]$ for near-term sail technology. From Fig. 19, one can infer for the latter interval of Γ_0 that at the upper limit $\varepsilon_\eta < 15\%$ for $\Delta\tau < 0.4$ years, whereas at the lower limit $\varepsilon_\eta < 5\%$ for $\Delta\tau < 1$ years. Because 0.4 years is a significantly long transfer time, we can conclude that the extrapolation method will be useful in the upcoming years while we move from current to near-term sail technology.

Finally, note that we presented the error analysis based on the best ascent case (i.e., the solid black line in Fig. 11a). We could have presented the exact same analysis for any of the other three reference performance curves that constitute the black $i = 90$ deg envelope (i.e., worst ascent, best descent, and worst descent). Nevertheless, the error with respect to the best ascent case is the largest, making the error contours in Fig. 19 a conservative estimate of the error contours for all other cases. Hereinafter, because of the latter reason, we apply Fig. 19 in general to all cases. However, note that there is a fundamental difference with respect to the error of the descent cases though. For the descent cases, the sign of the error is inverted: $\varepsilon_\eta > 0$ when $\Gamma_0 < G_0$, and $\varepsilon_\eta < 0$ when $\Gamma_0 > G_0$. When descending, $\rho < 1$, which causes the gravity term of order $\mathcal{O}(1/\rho^2)$ to become greater than one, reducing the effectiveness of the control, exactly the contrary effect that we discussed in the ascent case. In a nutshell, descending offers resistance, while ascending favors the ascent.

7.3. Examples

The extrapolation method can be used to estimate the performance of MC2C transfers in two different modes: 1) the *time mode* where, for a given target radius change $\Delta\rho$ we want to obtain the required transfer time $\Delta\tau$; and 2) the *range mode* where, for a given transfer time $\Delta\tau$, we want to obtain the achievable $\Delta\rho$. The workflow for both modes involves using the error equations Eqs. (21) and (22) together with Figs. 11 and 19. In addition, the method can be used for increasing (ascent) or decreasing (descent) the orbital radius, where the distinction is made in the sign of η, η_i, and $\Delta\rho$. The next two subsections explain in detail how to use the extrapolation method in the two different modes. Regardless of the mode, one needs to know: 1) the planet (P, μ); 2) the initial orbit (r_0, i); and 3) the performance of the sail (a_0).

7.3.1. Time mode

In the *time mode*, one obtains a conservative estimate of the best (minimum) and worst (maximum) transfer times ($\Delta\tau_b$, $\Delta\tau_w$) to reach a target radius change $\Delta\rho$. These best/worst transfer times constitute the transfer time envelope of the mission (i.e., for any initial phase ζ_0, the transfer time lies inside the envelope).

To use the *time mode*, the following steps need to be taken. 1) Compute $\Gamma_0 = a_0 P\sqrt{r_0/\mu}$. 2) Obtain the inverse reference performance $\eta_i = \Delta\rho\ G_0/\Gamma_0$. 3) Enter Fig. 11 (a for ascent and b for descent) with

η_i and retrieve the uncorrected best/worst times ($\Delta\tau_{i_b}$, $\Delta\tau_{i_w}$) from the curve closest to the input inclination i. 4) Find in Fig. 19 an adequate error level for each time ($|\varepsilon_{\eta_b}|$, $|\varepsilon_{\eta_w}|$), where the sign of the error is computed from $\varepsilon_\eta = |\varepsilon_\eta|\,\mathtt{sign}(\Gamma_0 - G_0)\,\mathtt{sign}(\Delta\rho)$. 5) Obtain the best/worst reference performances (η_b, η_w) by correcting η_i with the errors from the previous step as $\eta = \eta_i/(1+\varepsilon_\eta)$. 6) Lastly, enter Fig. 11 again with (η_b, η_w) to obtain the sought for ($\Delta\tau_b$, $\Delta\tau_w$)

To put the *time mode* into practice, we are going to analyze a hypothetical solar-sail debris removal mission around Earth ($\mu = 3.986004418\times10^5$ km^3/s^2, $P = 365.256$ days) using the parameters of the ACS3 solar sail ($a_0 = 0.045$ mm/s^2, mass $m = 16$ kg) [2]. The mission consists of two phases: 1) moving a debris object of 130 kg from GEO (i.e., $i = 23.44$ deg, $r_0 = 42{,}164$ km) to the graveyard orbit (i.e., $\Delta r = 300$ km), and 2) transferring from the graveyard orbit back to GEO. Note that during the first phase of the mission, the characteristic acceleration is reduced to $a_0 = 0.0049$ mm/s^2 due to the extra mass from the debris object.

To obtain the transfer time envelope for the first phase, we follow the steps detailed above: 1) for $a_0 = 0.0049$ mm/s^2 and $r_0 = 42{,}164$ km, $\Gamma_0 = 0.05$; 2) $\Delta\rho = 0.007$, which transforms to $\eta_i = 0.007\times0.51/0.05 = 0.07$; 3) enter Fig. 11a with $\Delta\rho = 0.07$ to obtain ($\Delta\tau_{i_b} = 0.38$, $\Delta\tau_{i_w} = 0.4$) years; 4) for an ascent transfer with $\Gamma_0 = 0.05$, we find in Fig. 19 that $\varepsilon_{\eta_b} = \varepsilon_{\eta_w} = -0.1$ is adequate for both uncorrected best/worst times; 5) $\eta_b = \eta_w = 0.07/(1-0.1) = 0.08$; 6) enter Fig. 11a with $\Delta\rho = 0.08$ to obtain the envelope for the first phase ($\Delta\tau_{b1} = 0.4$, $\Delta\tau_{w1} = 0.42$) years.

For the second phase: 1) the initial radius increases to $r_0 = 42{,}164 + 300$ km, and the debris is released (i.e., a_0 returns to 0.045 mm/s^2), yielding $\Gamma_0 = 0.46$; 2) $\Delta\rho = -0.007$, which transforms to $\eta_i = -0.007\times0.51/0.46 = -0.008$; 3) enter Fig. 11b with $\Delta\rho = -0.008$ to obtain ($\Delta\tau_{i_b} = 0.12$, $\Delta\tau_{i_w} = 0.16$) years; 4) because $\Gamma_0 \approx G_0$, the extrapolation error is negligible (i.e., $\varepsilon_{\eta_b} = \varepsilon_{\eta_w} = 0$); 5) $\eta_b = \eta_w = \eta_i = -0.008$; 6) the transfer time envelope for the second phase is ($\Delta\tau_{b2} = \Delta\tau_{i_b} = 0.12$, $\Delta\tau_{w2} = \Delta\tau_{i_w} = 0.16$) years.

As the final step, we add the transfer times of both phases to obtain the total mission envelope ($\Delta\tau_b = 0.52$, $\Delta\tau_w = 0.58$) years. It seems that, for this particular mission, the initial phase ζ_0 is not critical, as the difference between the worst and best total mission times is only 0.06 years (22 days). This hypothetical example shows that with just a calculator and Figs. 11 and 19, the mission designer can rapidly assess a large variety of mission scenarios without optimizing a single MC2C transfer, improving the workflow during early mission design.

To test the results, we numerically optimize two consecutive MC2C transfers, one for each phase of the mission. For the first transfer, $\Omega = 180$ deg and $i = 23.44$ deg are used, which represent a GEO orbit at the autumn equinox. For the second transfer, we take the final state of the first transfer as initial conditions, linking both trajectories. The first transfer achieves the desired radius increase of 300 km in 0.3925 years, whereas the second transfer, enhanced by the larger a_0, only takes 0.1592 years to return to GEO, yielding a total mission time of $\Delta\tau^* = 0.5517$ years. The optimal total mission time is contained in the envelope: $0.5517 \in (0.52, 0.58)$. Hence, the correctness of the extrapolation method in *time mode* is verified for this particular example.

7.3.2. Range mode

In the *range mode*, one obtains a conservative estimate of the worst (minimum) and best (maximum) radius changes ($\Delta\rho_w$, $\Delta\rho_b$) given a transfer time $\Delta\tau$. These worst/best radius changes constitute the range envelope of the mission (i.e., for any initial phase ζ_0, the achievable radius change lies in the envelope).

To use the *range mode*, the following steps need to be taken. 1) Compute $\Gamma_0 = a_0 P\sqrt{r_0/\mu}$. 2) Enter Fig. 11 (a for ascent and b for descent) with $\Delta\tau$ and retrieve the worst/best reference performances (η_w, η_b) from the curve closest to the input inclination i. 3) Find in Fig. 19 the error level $|\varepsilon_\eta|$ for Γ_0 and $\Delta\tau$, where the sign of the error is computed from $\varepsilon_\eta = |\varepsilon_\eta|\,\mathtt{sign}(\Gamma_0 - G_0)\,\mathtt{sign}(\Delta\rho)$. 4) Obtain the worst/best inverse reference performances (η_{i_w}, η_{i_b}) by correcting (η_w, η_b) with the error from the previous step as $\eta_i = \eta(1+\varepsilon_\eta)$. 5) Lastly, transform ($\eta_{i_w}$, η_{i_b}) to radius change with $\Delta\rho = \eta_i\,\Gamma_0/G_0$ to obtain the sought for range envelope ($\Delta\rho_w$, $\Delta\rho_b$)

To put the *range mode* into practice, consider a Sunjammer-type sail with $a_0 = 0.22$ mm/s^2 [1]. We would like to know by how much it can change its circular orbit radius in 0.4 years when starting from a MEO orbit with $r_0 = 15{,}000$ km and $i = 50$ deg. The sail can be used to ascend ($\Delta\rho > 0$) or descend ($\Delta\rho < 0$). Let us begin with the ascent case: 1) for the given a_0 and r_0, $\Gamma_0 = 1.35$; 2) Fig. 11a does not have an envelope for $i = 50$ deg, so we use the envelope for $i = 60$ (i.e., the closest envelope that would contain the envelope for $i = 50$ deg), which predicts ($\eta_w = 0.06$, $\eta_b = 0.13$); 3) for $\Gamma_0 = 1.35$ and $\Delta\tau = 0.4$ years, Fig. 19 indicates a positive error $\varepsilon_\eta = 0.25$ (positive because $\Delta\rho > 0$ and $\Gamma_0 > G_0$); 4) with the latter error, the worst/best inverse reference performances are ($\eta_{i_w} = 0.075$, $\eta_{i_b} = 0.1625$); 5) the inverse reference performances translate to the range envelope ($\Delta\rho_w = 0.2$, $\Delta\rho_b = 0.43$), which in physical units is ($\Delta r_w = 2952$ km, $\Delta r_b = 6397$ km).

For the descent, the *range mode* applies as follows: 1) $\Gamma_0 = 1.35$ as in the ascent case; 2) enter Fig. 11b with $\Delta\tau = 0.4$ to find ($\eta_b = -0.11$, $\eta_w = -0.055$); 3) because $\Delta\rho < 0$, the error $\varepsilon_\eta = -0.25$ becomes negative; 4) the best/worst inverse reference performances are ($\eta_{i_b} = -0.0825$, $\eta_{i_w} = -0.04125$); 5) the associated range envelope is ($\Delta\rho_b = -0.22$, $\Delta\rho_w = -0.11$), which in physical units is ($\Delta r_b = -3248$ km, $\Delta r_w = -1624$ km).

To test the validity of the results, two $\Delta\tau = 0.4$ years MC2C transfers (ascending and descending) with $\Omega = 0$ deg and $i = 50$ deg are optimized: the ascending transfer achieves $\Delta\rho^* = 0.3121$ ($\Delta r^* = 4682$ km) in 536 orbital revolutions, whereas the descending transfer achieves $\Delta\rho^* = -0.2124$ ($\Delta r^* = -3186$ km) in 799 orbital revolutions. Note that for both cases, the optimized results fall within the envelopes calculated with the extrapolation method: $4682\,\text{km} \in (2952,\ 6397)\,\text{km}$, and $-3186\,\text{km} \in (-3248,\ -1624)\,\text{km}$. Hence, the extrapolation method is validated in *range mode* for this specific example.

8. Limitations

It is important to discuss the main limitations of this work: idealized dynamics, infinite attitude control, and two-dimensional planar motion. We adopt the ideal sail model without eclipses and point-mass gravity. More realistic sail models exist [14], which predict lower solar-sail thrust for the same area-to-mass ratio. Hence, the performance of the MC2C transfers presented in this paper are rather optimistic. However, note that one can infer a correction factor to adjust the results; a more realistic sail can achieve the same MC2C performance as an ideal sail by increasing its area-to-mass ratio according to some correction factor. Concerning the control, for the worst cases, the ideal results indicate that large values of the cone angle are required to execute the worst MC2C transfers. Realistic sails might not be able to reach such large cone angles [21], rendering some of the worst transfers unfeasible.

Eclipses play a role for large values of the aspect angle β: the lower the orbit altitude and the closer the aspect angle to 90 deg, the larger the transfer fraction in eclipse. Thus, the results most affected by the no-eclipse assumption are the worst and low inclination transfers, respectively. Note that eclipses would introduce a coasting period every orbital revolution, which would increase the transfer time required to achieve the same performance; the conclusions regarding geometry and control would likely remain valid.

Additional gravitational perturbations, like the Earth's oblateness or third-body perturbations, would induce a precession of the line of nodes of the orbit. Such a precession would modify the evolution of the aspect angle (especially for very long transfers), changing the conditions for the initial phase angle in Eq. (19) for the best and worst transfer geometries. Even so, the explained logic to obtain the best and worst geometry would still apply, allowing the mission designer to analyze each particular case.

The assumed infinite attitude control ensures that the sailcraft is capable of instantaneously tracking the optimal sail orientation. In reality, because of the large moments of inertia, solar sails are not the most

agile spacecraft; depending on the particular design of the attitude control system, it is possible that some of the optimal control policies presented in this work cannot be realized. The lower the orbit, the faster the orientation has to change, given that the attitude rates of change are inversely proportional to the orbital period. However, note that preliminary analyses show that the required torque to follow the optimal sail orientation for transfers in the GEO region is below the millinewton-meter level, which can be achieved by the attitude control system of ACS3 [2].

Finally, regarding the two-dimensional planar assumption, the results do not change noticeably when the optimal control laws are propagated in three dimensions, suggesting that the conclusions drawn from two-dimensional dynamics also apply to three dimensions. The periodic nature of the control and the small solar-sail acceleration lead to negligible out-of-plane errors. Note that we do not consider any plane-change maneuvers in the results; thus, the performance envelopes cannot be used for missions requiring large plane-change maneuvers.

9. Conclusions

This paper characterizes planetocentric co-planar MC2C solar-sail transfers, where the achieved radius change $\Delta\rho$ in a fixed transfer time $\Delta\tau$ is used as the performance metric.

We identify the best and worst transfer geometries, which can be targeted by selecting an appropriate initial sun-orbit geometry. The initial sun-orbit geometry determines the subsequent evolution of the aspect angle β, which is defined as the angle between the angular momentum vector of the orbit and the sun-planet direction. It is found that when β is minimum at the midpoint of an MC2C transfer, performance is best; whereas when β is maximum at the middle of an MC2C transfer, performance is worst. Moreover, the difference between best and worst is largest when the orbital plane is perpendicular to the ecliptic plane (i.e., ecliptic inclination of $i = 90$ deg), and non-existent when $i = 0$ deg.

For the best geometry, convergence is fast because the optimizer takes advantage of the natural dynamics for orbit raising and circularization; the set of feasible controls is used in full, yielding the best performance. Conversely, for the worst geometry, no natural circularization phase exists, forcing the optimizer to find a more complex control law that misuses the set of feasible controls, yielding the worst performance. Moreover, there is a particular geometry, coined the *self-transfer* geometry, for which no optimization is needed: a locally optimal orbit raising maneuver is sufficient to achieve an MC2C transfer.

By exploiting the best and worst transfer geometries, we define the performance envelopes that relate performance $\Delta\rho$ with transfer time $\Delta\tau$ (or vice versa) without the need for numerical optimization. The envelopes are presented in scaled units, so that they can be used to rapidly link $\Delta\rho$ with $\Delta\tau$ for any MC2C transfer around any planet in the solar system.

To extrapolate the envelopes to any set of initial conditions, a new parameter is introduced, Γ_0, that represents a measure of the control authority of the sail during a planetocentric trajectory. Two MC2C transfers with the same value for Γ_0 and the same orbital plane geometry, share the same transfer structure and yield the same performance. Hence, the envelopes that are computed around Earth for one value of Γ_0 are also applicable to any set of parameters around any planet that yield the same value of Γ_0. Additionally, we present an extrapolation method to obtain envelopes for other values of Γ_0. The extrapolation error is analyzed to understand the domain of the method (i.e. how far can one move away from the reference Γ_0); a systematic approach that corrects for the extrapolation error is presented and demonstrated, further enhancing the usability of the performance envelopes.

Finally, the indirect formulation adopted in this work proved to be very robust; almost all optimizations converged with a trivial initial guess. The fact that the dimension of the optimization problem is always fixed, renders the indirect method ideal to deal with the many-revolutions of an MC2C transfer (e.g., we achieved convergence up to 19,739 revolutions). Furthermore, the software implementation (available online [25]) uses automatic differentiation to compute the co-state dynamics; the code can therefore be easily adapted to handle more complex dynamical models, which we encourage the reader to try.

CRediT authorship contribution statement

Fernando Gámez Losada: Writing – original draft, Visualization, Validation, Software, Project administration, Methodology, Investigation, Formal analysis, Conceptualization; **Oskar Miller:** Visualization, Validation, Software, Methodology; **Pieter Visser:** Writing – review & editing, Supervision; **Jeannette Heiligers:** Writing – review & editing, Supervision, Project administration, Funding acquisition.

Declaration of competing interest

The authors declare that they have no known competing financial interests or personal relationships that could have appeared to influence the work reported in this paper.

Acknowledgements

This work was funded by a Vidi Grant of the Dutch Research Council (NWO), Project Number 19690: SWEEP – Space-Waste Elimination around Earth by Photon Propulsion.

Data availability

The code is publicly available in a GitHub repository that is referenced in the manuscript.

References

[1] M. Berthet, J. Schalkwyk, O. Çelik, D. Sengupta, K. Fujino, A.M. Hein, L. Tenorio, J. Cardoso dos Santos, S.P. Worden, P.D. Mauskopf, Y. Miyazaki, I. Funaki, S. Tsuji, P. Fil, K. Suzuki, Space sails for achieving major space exploration goals: historical review and future outlook, Prog. Aerosp. Sci. 150 (2024) 101047. https://doi.org/10.1016/j.paerosci.2024.101047

[2] W.K. Wilkie, Overview of the NASA advanced composite solar sail system (ACS3) technology demonstration project, in: AIAA Scitech 2021 Forum, American Institute of Aeronautics and Astronautics, 2021. https://doi.org/10.2514/6.2021-1260

[3] V.L. Coverstone, J.E. Prussing, Technique for escape from geosynchronous transfer orbit using a solar sail, J. Guid. Contr. Dyn. 26 (4) (2003) 628–634. https://doi.org/10.2514/2.5091

[4] G. Mengali, A.A. Quarta, Earth escape by ideal sail and solar-photon thrustor spacecraft, J. Guid. Contr. Dyn. 27 (6) (2004) 1105–1108. https://doi.org/10.2514/1.10637

[5] M. Macdonald, C.R. McInnes, Realistic earth escape strategies for solar sailing, J. Guid. Contr. Dyn. 28 (2) (2005) 315–323. https://doi.org/10.2514/1.5165

[6] G. Mengali, A.A. Quarta, Near-optimal solar-sail orbit-raising from low earth orbit, J. Spacecr. Rockets 42 (5) (2005) 954–958. https://doi.org/10.2514/1.14184

[7] L. Carzana, P. Visser, J. Heiligers, Locally optimal control laws for earth-bound solar sailing with atmospheric drag, Aerosp. Sci. Technol. 127 (2022) 107666. https://doi.org/10.1016/j.ast.2022.107666

[8] V. Stolbunov, M. Ceriotti, C. Colombo, C.R. McInnes, Optimal law for inclination change in an atmosphere through solar sailing, J. Guid. Contr. Dyn. 36 (5) (2013) 1310–1323. https://doi.org/10.2514/1.59931

[9] R.M. Fitzgerald, Characterizing minimum-time solar sail geostationary orbit transfers using pseudospectral optimal control, J. Spacecr. Rockets 58 (4) (2021) 997–1009. https://doi.org/10.2514/1.A34950

[10] P. Kelly, R. Bevilacqua, Geostationary debris mitigation using minimum time solar sail trajectories with eclipse constraints, Optim. Contr. Appl. Methods 42 (1) (2020) 279–304. https://doi.org/10.1002/oca.2676

[11] C. Bianchi, L. Niccolai, G. Mengali, M. Ceriotti, Preliminary design of a space debris removal mission in LEO using a solar sail, Adv. Space Res. (2024). https://doi.org/10.1016/j.asr.2024.01.024

[12] L.L. Sackett, Optimal Solar Sail Planetocentric Trajectories, Tech. Rep. NASA-CR-157130, NASA, 1977.

[13] K. Oguri, G. Lantoine, A.E. Petropoulos, J.W. McMahon, Solar sailing Q-law for planetocentric, many-revolution sail orbit transfers, J. Guid. Contr. Dyn. 46 (10) (2023) 2005–2014. https://doi.org/10.2514/1.G007103

[14] C.R. McInnes, Solar Sailing: Technology, Dynamics and Mission Applications, Springer Science & Business Media, 2004.

[15] J.A.E. Bryson, Y.-C. Ho, Applied Optimal Control: Optimization, Estimation and Control, CRC Press, Cambridge, 1st edition edition, 1975.
[16] K. Oguri, G. Lantoine, J.W. McMahon, Solar sailing primer vector theory: indirect trajectory optimization with practical mission considerations, J. Guid. Contr. Dyn. 45 (1) (2022) 153–161. https://doi.org/10.2514/1.G006210
[17] D. Morante, M.S. Rivo, M. Soler, A survey on low-thrust trajectory optimization approaches, Aerospace 8 (3) (2021) 88. https://doi.org/10.3390/aerospace8030088
[18] O. Miller, Indirect Optimization of Planetocentric Solar Sail Trajectories for Circular Orbit Transfers, Master's thesis, Delft University of Technology, 2025.
[19] F. Gámez Losada, P. Visser, J. Heiligers, Estimating the performance of patched multirevolution solar-sail transfers around planets, J. Guid. Contr. Dyn. (2025) 1–12. https://doi.org/10.2514/1.G009233
[20] J.M. Longuski, J.J. Guzmán, J.E. Prussing, Optimal Control with Aerospace Applications, Springer New York, 2014. https://doi.org/10.1007/978-1-4614-8945-0
[21] G. Mengali, A.A. Quarta, Optimal three-dimensional interplanetary rendezvous using non-ideal solar sail, J. Guid. Contr. Dyn. 28 (1) (2005) 173–177. https://doi.org/10.2514/1.8325
[22] P. Kidger, On Neural Differential Equations, Ph.D. thesis, University of Oxford, 2021.
[23] M. Blondel, Q. Berthet, M. Cuturi, R. Frostig, S. Hoyer, F. Llinares-López, F. Pedregosa, J.-P. Vert, Efficient and modular implicit differentiation, Adv. Neural Inf. Process. Syst. 35 (2022) 5230–5242.
[24] P. Virtanen, R. Gommers, T.E. Oliphant, M. Haberland, T. Reddy, D. Cournapeau, E. Burovski, P. Peterson, W. Weckesser, J. Bright, S.J. van der Walt, M. Brett, J. Wilson, K.J. Millman, N. Mayorov, A.R.J. Nelson, E. Jones, R. Kern, E. Larson, C.J. Carey, İ. Polat, Y. Feng, E.W. Moore, J. VanderPlas, D. Laxalde, J. Perktold, R. Cimrman, I. Henriksen, E.A. Quintero, C.R. Harris, A.M. Archibald, A.H. Ribeiro, F. Pedregosa, P. van Mulbregt, SciPy 1.0 Contributors, SciPy 1.0: fundamental algorithms for scientific computing in python, Nat. Methods 17 (2020) 261–272. https://doi.org/10.1038/s41592-019-0686-2
[25] O. Miller, F. Gámez Losada, Code for Characterization of Multi-Revolution Circular-to-Circular Solar-Sail Transfers Around Planets, 2026, https://github.com/fer202122/indirecpublic. https://doi.org/10.4121/36e472de-7ccf-44b4-b3fa-7215d094faf1
[26] F. Gámez Losada, P. Visser, J. Heiligers, Fundamentals of circular-to-circular solar-sail transfers around planetary bodies, Adv. Space Res. (2026). https://doi.org/10.1016/j.asr.2026.02.049